Photoacoustics 20 (2020) 100207

Contents lists available at ScienceDirect

Photoacoustics

journal homepage: www.elsevier.com/locate/pacs

Review article

# Towards non-contact photoacoustic imaging [review]

Zohreh Hosseinaee [a], Martin Le [a], Kevan Bell [a,b], Parsin Haji Reza [a,*]

[a] PhotoMedicine Labs, Department of System Design Engineering, University of Waterloo, Ontario, N2L 3G1, Canada
[b] IllumiSonics Inc., Department of Systems Design Engineering, University of Waterloo, Waterloo, Ontario, N2L 3G1, Canada

ARTICLE INFO

*Keywords:*
Photoacoustic imaging
Photoacoustic microscopy
All-optical photoacoustic
Non-contact photoacoustic

ABSTRACT

Photoacoustic imaging (PAI) takes advantage of both optical and ultrasound imaging properties to visualize optical absorption with high resolution and contrast. Photoacoustic microscopy (PAM) is usually categorized with all-optical microscopy techniques such as optical coherence tomography or confocal microscopes. Despite offering high sensitivity, novel imaging contrast, and high resolution, PAM is not generally an all-optical imaging method unlike the other microscopy techniques. One of the significant limitations of photoacoustic microscopes arises from their need to be in physical contact with the sample through a coupling media. This physical contact, coupling, or immersion of the sample is undesirable or impractical for many clinical and pre-clinical applications. This also limits the flexibility of photoacoustic techniques to be integrated with other all-optical imaging microscopes for providing complementary imaging contrast. To overcome these limitations, several non-contact photoacoustic signal detection approaches have been proposed. This paper presents a brief overview of current non-contact photoacoustic detection techniques with an emphasis on all-optical detection methods and their associated physical mechanisms.

## 1. Introduction

Photoacoustic imaging (PAI) is an impactful modality in biomedical optics that has attracted interest from various research communities in the last decade, especially biomedical imaging. Historically, the photoacoustic effect was discovered by Bell in 1880 [1]. He discovered that sound waves might be generated in solid material when exposed to a pulsed light source. Development of the laser in the 1960s had a significant impact on the field by providing directional, high peak power, and spectrally pure beam that many photoacoustic applications require. Subsequently, the phenomena found popularity in spectroscopy, and in 1964 Amar et al. reported the application of PA spectroscopy for *in-vivo* rabbit eye [2] and ex-vivo human eye specimens [3]. Theodore Bowen was among the first to propose the phenomena for soft tissue imaging in 1981 [4]. These early studies progressed, culminating in work published in 1993 which demonstrated one of the first *in-vivo* photoacoustic study performed on human finger [5]. Thereafter, the field has seen significant advancements in terms of instrumentation, image reconstruction algorithms, functional imaging, and molecular imaging capabilities.

PAI offers high sensitivity for obtaining optical absorption contrast over a wide range of spatial scales from organelles, cells, tissue, organs, and small animals. Additionally, it is complementary to other imaging modalities in terms of contrast, sample penetration, spatial and temporal resolutions. These unique opportunities were utilized in the last two decades in several pre-clinical and clinical applications including but not limited to, blood oxygen saturation imaging [6–8], brain vasculature and functional imaging [9–11], gene expression [12], vulnerable atherosclerotic plaques diagnosis [13], skin melanomas [14], histology-like tissue imaging [15,16], longitudinal tumor angiogenesis studies [17], imaging and detection of protein interactions [18], multi-modal ocular imaging [19–22], and tissue engineering scaffolds [23,24]. In addition, PAI methods have been utilized in different non-medical applications such as non-destructive testing [25,26] detecting metal surface defects [27], spectroscopy [28,29], and uncovering hidden features in paintings [30].

## 2. Physical mechanism of photoacoustic imaging

In general, when biological tissues are irradiated by photons of light, depending on the light wavelength, the photons penetrate to some depths. Inside the tissue, these photons get scattered and absorbed, where the absorption occurs by light-absorbing molecules known as chromophores. The absorbed optical energy induces a local transient temperature rise, which generates pressure via thermo-elastic

* Corresponding author.
*E-mail address:* phajireza@uwaterloo.ca (P.H. Reza).

https://doi.org/10.1016/j.pacs.2020.100207
Received 18 May 2020; Received in revised form 29 June 2020; Accepted 10 July 2020
Available online 23 September 2020

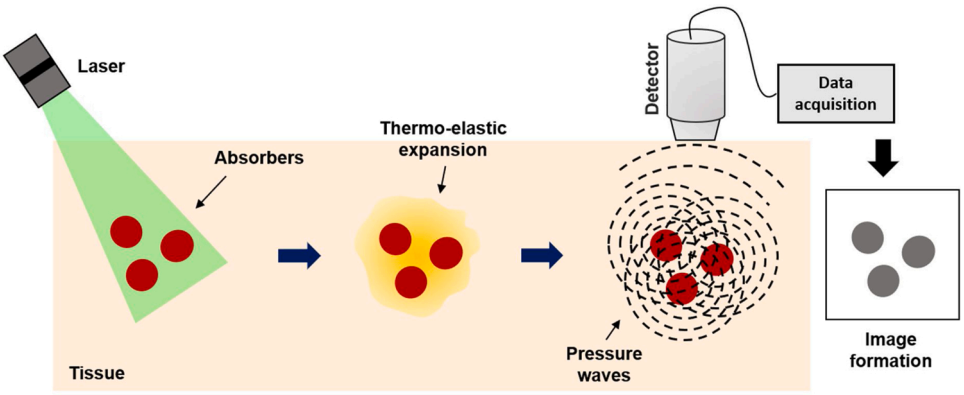


**Fig. 1.** General principle of photoacoustic imaging. Targeted chromophores absorb optical energy resulting in a local temperature rise, inducing local pressure rise, which propagates outwards towards an ultrasonic transducer. The recorded signal is reconstructed to map the original optical energy deposition inside the tissue.

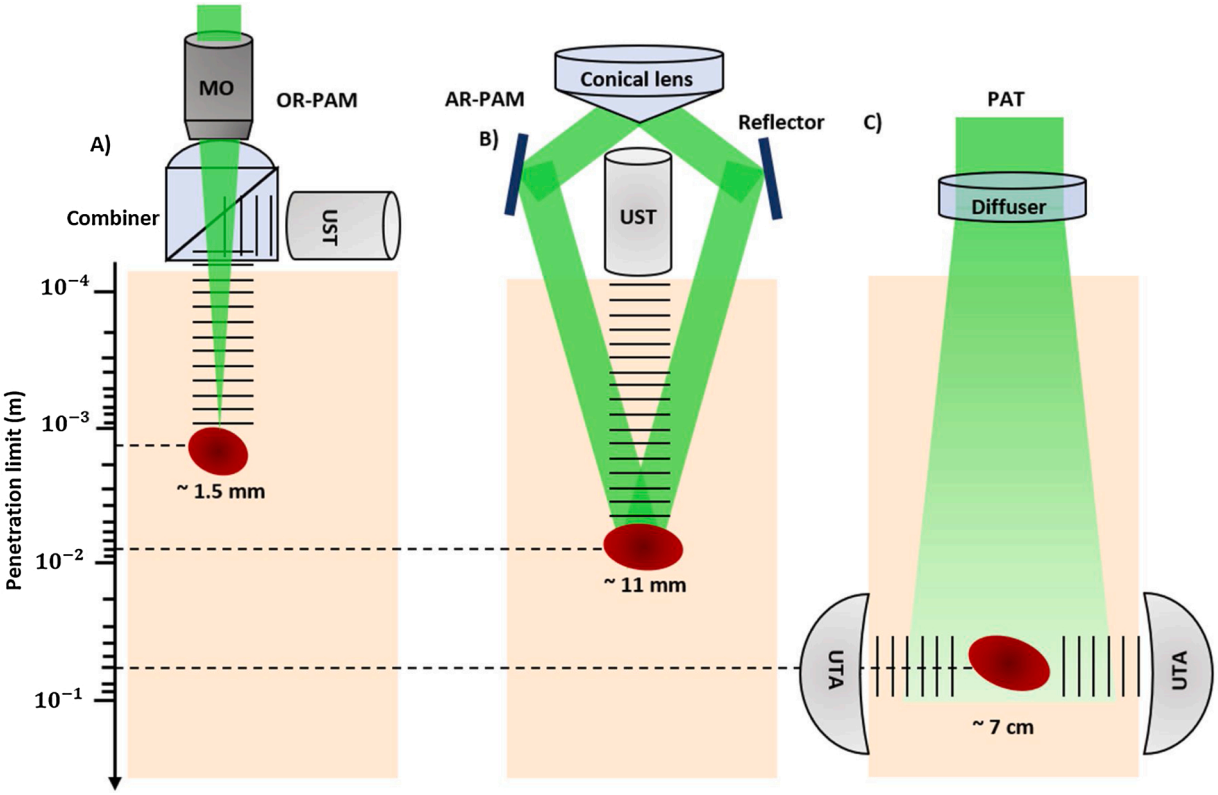


**Fig. 2.** Signal generation and detection in different implementations of PAI with different penetration limits in scattering tissue. These depths values are the maximum depths reported in the literature. **(a)** Reflection-mode OR-PAM system with an optical–acoustic combiner that transmits light but reflects sound. OR-PAM system with 1.5 mm imaging depth was reported [65]. **(b)** AR-PAM system where the laser light is only weakly focused, previous work demonstrated 11 mm imaging depth in biological tissue [61]. **(c)** PAT system with a ring-shaped ultrasonic transducer array (UTA). The laser beam is expanded and homogenized by a diffuser to provide widefield illumination. Recent research has proved 7 cm imaging depth achieved in biological tissue [40].

expansion. In thermal confinement the photoacoustic equation for an arbitrary absorbing target with an arbitrary excitation source is defined as [31]:

$$\left(\nabla^2 - \frac{1}{v_s^2}\frac{\partial^2}{\partial t^2}\right)p(\vec{r},t) = -\frac{\beta}{C_p}\frac{\partial H}{\partial t} \quad (1)$$

Where $p(\vec{r},t)$ denotes the acoustic pressure rise at location $\vec{r}$ at time $t$, $v_s$ is the speed of sound, β is the thermal coefficient of volume expansion, $C_p$ denotes the specific heat capacity at constant pressure, and $H$ represents the heating function defined as the thermal energy deposited per unit volume and per unit time [32]. Based on this equation, photoacoustic pressure propagation is driven by the first-time derivative of the heating function. Therefore, time-invariant heating does not generate photoacoustic pressure waves. When both thermal and stress confinements are met, thermal expansion causes a pressure rise ($p_0$) that can be estimated by [33]:

$$p_0 = \Gamma.\mu_a.F \quad (2)$$

Where $p_0$ is the initial pressure rise, $\mu_a$ is the absorption coefficient ($\frac{1}{cm}$), $\Gamma = \beta v_s^2/C_p$ is the Grüneisen coefficient [34,35] representing thermal and mechanical properties of the tissue, and $F$ is the fluence of the irradiated energy ($\frac{J}{cm^2}$). According to the American National Standard

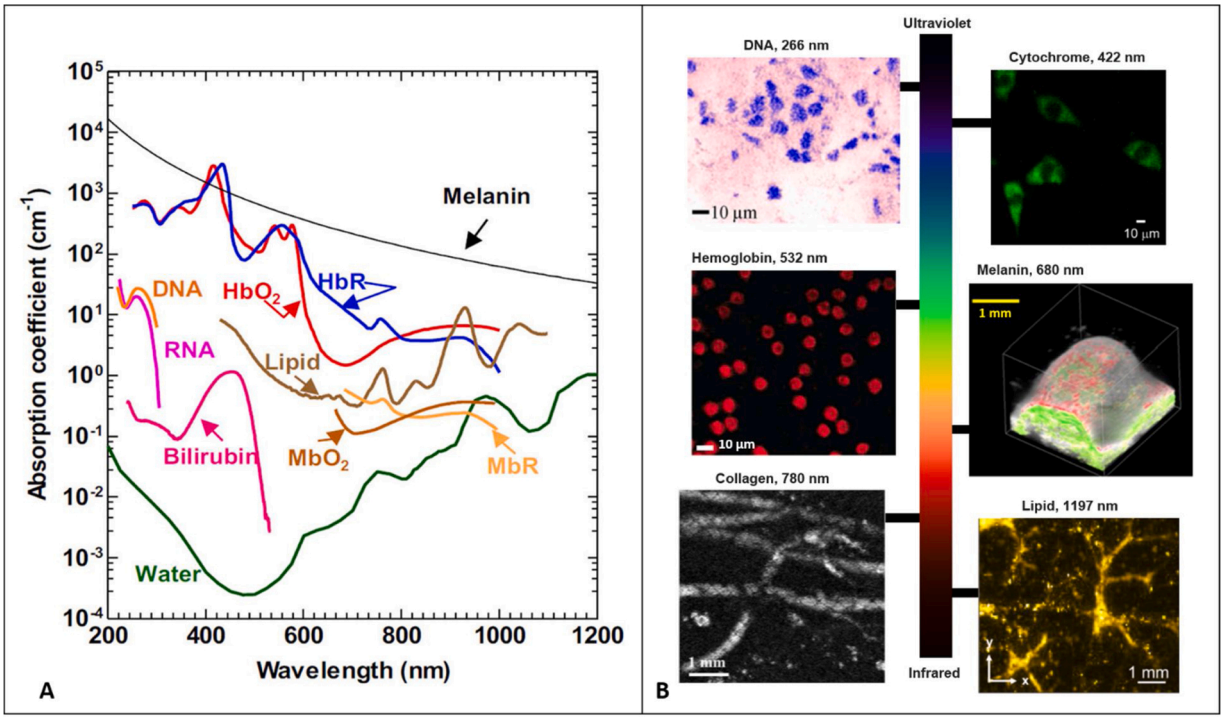


**Fig. 3.** **(A)** Absorption spectra of common endogenous chromophores in biological tissues. Reprinted with permission from [36] **(B)** photoacoustic images acquired from mouse small intestine cells and DNA contrast at 266 nm. Reprinted with permission from [79], fibroblast cytoplasm's with cytochrome contrast at 422 nm, reprinted with permission from [80], PA image of mouse blood smear with hemoglobin contrast at 532 nm, reprinted with permission from [81], tyrosinase tumor expressing with melanin contrast at 680 nm, reprinted with permission from [12], photoacoustic image of mouse paw with skin removed and collagen contrast at 780 nm, reprinted with permission from [82], intramuscular fat photoacoustic image with lipid contrast at 1197 nm, reprinted with permission from [83].

Institute (ANSI) safety standard, in the visible spectral region, the maximum permissible fluence on the skin surface is 20 $mJ/cm^2$. The generated pressure propagates in the form of acoustic waves and can be detected on the surface of the tissue by an ultrasonic transducer or transducer array. These signals form an image that maps the optical energy absorption inside the tissue [36] (Fig. 1).

## 3. Photoacoustic modalities

PAI can be split into two main categories depending on how the images are formed: photoacoustic tomography (PAT), which uses reconstruction-based image formation and photoacoustic microscopy (PAM), which uses focused-based image formation (Fig. 2).

In PAT, an unfocused optical beam excites the region of interest, and an array of ultrasonic transducers measures the generated ultrasound waves in multiple positions [37–40]. Common detection geometries used in PAT are planar, cylindrical, and spherical. In planar detection mode, a two-dimensional planar, linear, or phased array is used, while cylindrical detection mode uses ring transducer arrays or split ring arrays [41,42]. Spherical detection has been used for imaging with an arc-shaped transducer array [43,44] and a hemispherical array [45,46]. The axial resolution of a PAT system is defined by the bandwidth of the detector, while the lateral resolution is dependent on the detection geometries [47]. PAT imaging depth theoretically is limited to ~10 cm in soft tissue, where the optical fluence is significantly attenuated due to both absorption and scattering [48]. Previous works have demonstrated 720 μm lateral resolution at a depth of ~7 cm in biological tissue [40]. PAT can be used for various applications ranging from microscopic to macroscopic imaging, and it can provide large field of view (FOV) images. As a result, it has been used in applications such as whole-body imaging of small animals [49] and clinical breast cancer studies [50].

Unlike PAT, PAM employs raster-scanning of optical and acoustic foci and forms images directly from recorded depth-resolved signals [51]. PAM is generally used for applications that require high-resolution rather than deep penetration depth like single-cell imaging [52]. PAM can be further classified into acoustic-resolution PAM (AR-PAM), where the acoustic focusing is tighter than optical focusing [53], and optical-resolution PAM (OR-PAM), where the optical focusing is tighter [54,55].

### 3.1. Acoustic resolution photoacoustic microscopy (AR-PAM)

For AR-PAM, a poorly focused beam of light illuminates the tissue, and the induced photoacoustic signals are detected using a focused ultrasound transducer. Since the acoustic focus is limited by the acoustic diffraction limit rather than the optical diffraction limit, the achieved resolution by AR-PAM is on the order of tens of microns [56]. The lateral resolution of AR-PAM is given by [57]:

$$\Delta x_{AR-PAM} = 0.71\lambda_a / NA_a \tag{3}$$

Where $\lambda_a$ is the acoustic wavelength, and $NA_a$ is the numerical aperture (NA) of the focused ultrasonic transducer. The axial resolution of PAT and AR-PAM is determined by the bandwidth $(\Delta f)$ of the ultrasonic transducer, which can be described as [58]:

$$\Delta z = 0.88c/\Delta f \tag{4}$$

where c is the speed of sound. AR-PAM has been used for the deep-penetration imaging of microvasculature [59] and functional brain imaging with improved penetration depth [60]. For example, an imaging depth of ~ 11 mm has been demonstrated in biological tissue, which is ~10 times higher than the attainable depth of OR-PAM [61]. Another example comes from Moothanchery et al. [62], who reported an AR-PAM system with a lateral resolution of 45 μm with an imaging depth of ~7.6 mm for deep vasculature imaging.

### 3.2. Optical resolution photoacoustic microscopy (OR-PAM)

The resolution of OR-PAM is limited by the optical diffraction limit of the focused laser beam [63]. Therefore it generates images with higher resolution than AR-PAM; however its penetration depth is restricted by the optical transport mean free path, which is ~ 1.5 mm for visible wavelengths in biological tissues [64,65]. The lateral resolution of OR-PAM can be defined as [55]:

$$\Delta x_{OR-PAM} = 0.51\lambda_o/NA_o \quad (5)$$

where $\lambda_o$ is the optical wavelength and $NA_o$ is the NA of the objective lens. In an OR-PAM configuration, the axial and lateral resolutions are defined by the NA of the objective lens. The high lateral resolution makes OR-PAM suitable for a wide range of applications. Zhang et al. [52] reported the first subwavelength OR-PAM by employing a 1.23 NA objective lens, obtaining a lateral resolution of 0.22 μm. Here, single-cell imaging was demonstrated on individual melanoma cells and erythrocytes.

## 4. Imaging contrast

Photoacoustic imaging modalities offer a unique imaging contrast by taking advantage of direct optical absorption. In other words, any imaging target that absorbs light energy, can be visualized by PAI modalities. In biological tissues, both endogenous and exogenous contrast agents can be exploited as imaging targets. Endogenous contrast agents are ideal targets as they are naturally available in tissue. Therefore, they are non-toxic and do not interfere with the original tissue microenvironment. The most commonly imaged endogenous contrast agents for PAI include DNA/RNA, hemoglobin, melanin, lipids, collagen, and water (Fig. 3). Among these, DNA/RNA is commonly used for cell nuclei imaging using an ultraviolet excitation source [66], hemoglobin is widely used for vascular imaging in the visible and near-infrared (NIR) spectral ranges [63], and melanin is used for melanoma tumor imaging in the NIR region [67]. Additionally, in the NIR region, lipids and water are used for atherosclerotic plaque [68] and injury imaging [69], respectively. Since these endogenous contrast agents have different absorption spectra, PAI can differentiate them with spectral measurements when the local optical fluence is known [70]. Exogenous contrast agents also offer the ability to be specifically engineered for maximum detection sensitivity and can be conjugated with target molecules to selectively bind to specific cell surface receptors [71,72]. Their performance has been demonstrated for several applications such as cancer imaging [73,74], functional brain imaging [75,76], and monitoring therapeutic procedures [77,78].

## 5. Photoacoustic signal detection

Photoacoustic signals can be generated by an intensity-modulated continuous-wave (CW) excitation [84] or pulsed excitation [59]. Pulse excitation is more commonly used, since the signal-to-noise ratio (SNR) of photoacoustic signal is higher than that in CW excitation, if the same number of photons are delivered, or ANSI safety limits are considered [85]. Photoacoustic signals are broadband and thus demand the use of wideband ultrasonic transducers. The center frequency and bandwidth of the detector are two significant parameters, and, based on the intended application, the appropriate center frequency and bandwidth must be selected. Popular types of ultrasonic transducers for photoacoustic signal detection include piezoelectric transducers, Fabry-Perot interferometers (FPI), capacitive micromachined ultrasound transducers (CMUTs), and micro ring resonators (MRRs) [37].

Despite offering several advantages, ultrasonic transducers need to be physically in contact with the sample through a coupling medium. Contact-based detection minimizes acoustic reflection losses at poorly matched interfaces such as between tissue and air. This poorly matched interface would result in pressure wave reflections back into the sample and away from the acoustic transducer. Appropriate acoustic matching is required to produce a conventional PAI device with high sensitivity. Physical contact, coupling, or immersion is not suitable for some applications. For example, ophthalmic imaging applications cannot fully benefit from PAI for structural and functional microvasculature visualization. Currently, in ophthalmic applications, the ultrasonic transducer is placed on the surface of the tissue or conjunctiva [86], increasing the risk of abrasion, infection, and patient discomfort. Additionally, involuntary eye movements may affect the coupling efficiency and degrade image quality [87,88]. In small animal imaging, immersion in water significantly complicates the procedure and commonly results in sacrificing the animal [87,89].

Although the skin is potentially the most accessible organ for optical and acoustic imaging, and PAI can be used for clinical dermatological applications, the requirement of physical contact, as opposed to purely optical methods, poses some limitations. In wound assessment and burn diagnostics, a coupling medium and physical contact with the sample increases the risk of infection.

Endoscopic applications would also benefit from a non-contact detection mechanism [90–92]. At the moment, most photoacoustic endoscopic systems use miniaturized piezoelectric transducers, which complicate the design of the endoscopic tip due to their size and opaque nature. The sensitivity and FOV of these transducers will be sacrificed by shrinking their size which adversely effect the achieved image quality. In addition, these transducers require direct contact and an impedance matching medium, resulting in an obstructed view, restricting their imaging capabilities to rotational scanning and side-views. Therefore, the advantages of forward-view imaging for guiding minimally invasive surgical procedures and special imaging applications are not available [93].

Additionally, in brain imaging, when applied to surgical applications, the transducer array must be inserted in a sterile saline solution, which acts as the coupling medium. To keep the solution stable and maintain maximum efficiency, it requires a horizontal working plane which is not convenient to achieve when the patient is on a surgical bed [91].

Moreover, most ultrasound detectors are opaque, which restricts the illumination direction of the excitation laser beam so that the inline configuration of detector and laser is challenging. Furthermore, combining PAI systems with other optical imaging modalities may require a complicated design. Therefore, a non-contact detection approach that avoids these issues opens up new possibilities for clinical applications and multi-modal imaging techniques [94–96].

Several techniques have been developed to realize non-contact detection of photoacoustic signals. Air-coupled transducers and all-optical detection methods such as interferometric- and non-interferometric-based approaches have been proposed as alternatives to contact-based ultrasonic transducers. Here, an overview of these techniques and their underlying physical mechanisms and reconstruction algorithms are presented.

## 6. Non-contact photoacoustic signal detection

### 6.1. Air-Coupled detection

Coupling transducers through air/gas has been explored to eliminate the need to use coupling media in conventional ultrasound transducers. The approach has been used for a wide range of ultrasound imaging applications, including non-destructive testing [97–100], material characterization [101–103], secure wireless transmission of data [104], sensing and analysis of cultural heritage [105], water control in agriculture [106,107], quality control in food industry [108] and computer gesture-base control [109,110]. A major drawback of the air-coupled ultrasound transducers comes from the impedance mismatch between air and solids, which cause high attenuation of ultrasound signal in the

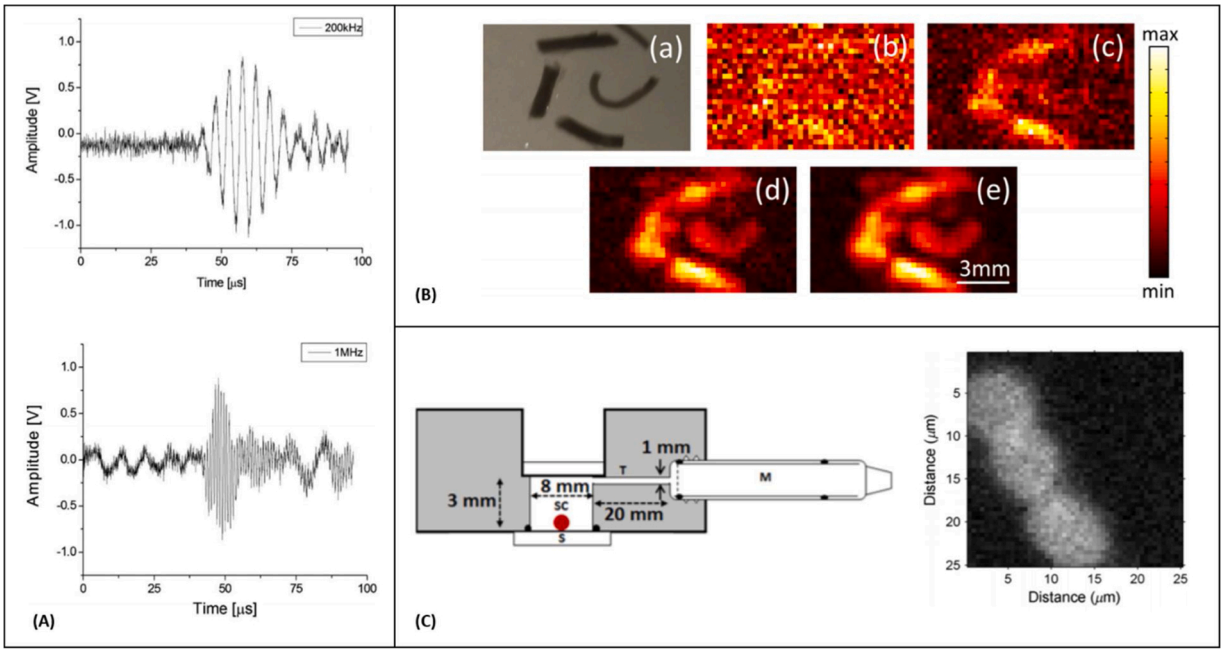


**Fig. 4.** **(A)** Photoacoustic time traces from an artificial blood vessel, recorded with air-coupled ultrasound transducers with center frequency of 200 kHz and 1 MHz (the recorded signals are averaged 512 times), reprinted with permission from [120] **(B)** Photoacoustic images obtained by raster scanning of the air-coupled transducer (a) Photograph of the imaged ink channels. (b)–(e) Photoacoustic images of the phantom after the recorded signals have been averaged 1, 10, 100, and 1000 times respectively, Reprinted from [121], with the permission of AIP Publishing. **(C)** Schematic diagram of the PA sensor and PA images of red blood cells smeared on a glass substrate, M is the microphone, SC is the sample chamber, S is substrate, reprinted with permission from [122].

air [111]. Therefore, applications mentioned earlier were possible through improving the design of air-coupled transducers [112–115], increasing the excitation energy, low noise amplification, and digital signal processing techniques [116–119]. In addition, to further reduce losses and maintain a reasonable SNR, the working frequency is usually below 1 MHz, which is relatively low compared to the tens of MHz frequency range of common ultrasound transducers used in medical photoacoustic imaging applications.

In 2010, Kolkman et al. [120] demonstrated the feasibility of air-coupled transducers to detect photoacoustic signals in artificial blood vessels made of a silicon rubber tube filled with human blood. Here, the excitation fluence satisfied the ANSI maximum permissible exposure (MPE) limits and the energy density at the interface was of about 20 $mJ/cm^2$. Two unfocused transducers with central frequencies at 200 KHz and 1 MHz were placed at 7.5 mm above the phantom interface and recorded photoacoustic time traces (Fig. 4A). The achieved axial resolution of their system was measured as 13 mm for 200 KHz transducer and 4 mm for the 1 MHz one. In 2015, Dean-Ben et al. [121] developed a transmission mode PAI system using a custom-designed air-coupled piezoelectric transducer with a central frequency of 800 kHz and bandwidth of 400 kHz. Their experiment followed the excitation light fluence determined by the ANSI safety limits, however, the narrow detection bandwidth of the transducer significantly compromised the system's resolution performance. Images of vessel-mimicking tubes were acquired; and significant averaging was found necessary to properly resolve these structures (Fig. 4B). Sathiyamoorthy et al. [122] developed an inverted photoacoustic microscope using a low-power CW laser and a kHz-range microphone. Information about the incident power on the imaging sample was not reported for this study. The detector was attached to a custom-designed chamber, and images from red blood cells located inside the chamber were recorded with a lateral resolution of 1.37 μm (Fig. 4C). The need for mechanical scanning and a large ensemble of averaging inhibit potential *in-vivo* applications of the air-coupled transducers due to their long acquisition time.

### 6.2. *Optical detection of photoacoustic signals*

Early studies on optical detection of ultrasound signal began in 1960s [123]. In the last decade, due to the advancement of material science and fabrication technologies, significant progress has been made in developing high-performance optical detectors for ultrasound signals [124]. Optical ultrasound detection methods provide higher sensitivity, and wider frequency bandwidth over conventional piezoelectric devices, and also offer the opportunity of developing miniaturized and optically transparent ultrasound detectors [125]. Contact-based optical photoacoustic detectors like polymer microring resonators and FPIs have been widely used in applications such as bladder tissue vasculature imaging [126], *in-vivo* imaging of the vasculature in human skin [127–130], endoscopic imaging of microvasculature [131,132] and multi-modal imaging [133,134]. Furthermore, all-optical PAM system based on pressure distribution measurements and probe beam deflection techniques were developed, despite offering high sensitivity and micron scale resolution in these method the sample needs to be submerged in water cell limiting the *in-vivo* applications [135–138].

#### 6.2.1. *Speckle pattern analysis*

Speckle is a feature of coherent light propagation formed when interference occurs between superimposed waves [139]. This effect has been leveraged in several techniques, including laser speckle imaging [140], ultrasonography [141], synthetic aperture radar [142], and optical coherence tomography [143]. When photoacoustic waves arrive at the sample surface, they cause mechanical deformations. When a continuous-wave laser illuminates this region, these surface deformations modulate the speckle patterns of the backscattered beam. By characterizing these patterns, information about the surface deformations, and thus the acoustic pressure, can be extracted [144–148].

In 1999, Leveque et al. [149] developed a speckle detection scheme where a CCD camera operated as a detector array. This technique could demonstrate one-dimensional images of biological tissue. The system was further modified for acquiring two-dimensional and three-dimensional images [150–154] (Fig. 5A). Horstmann et al. [155]

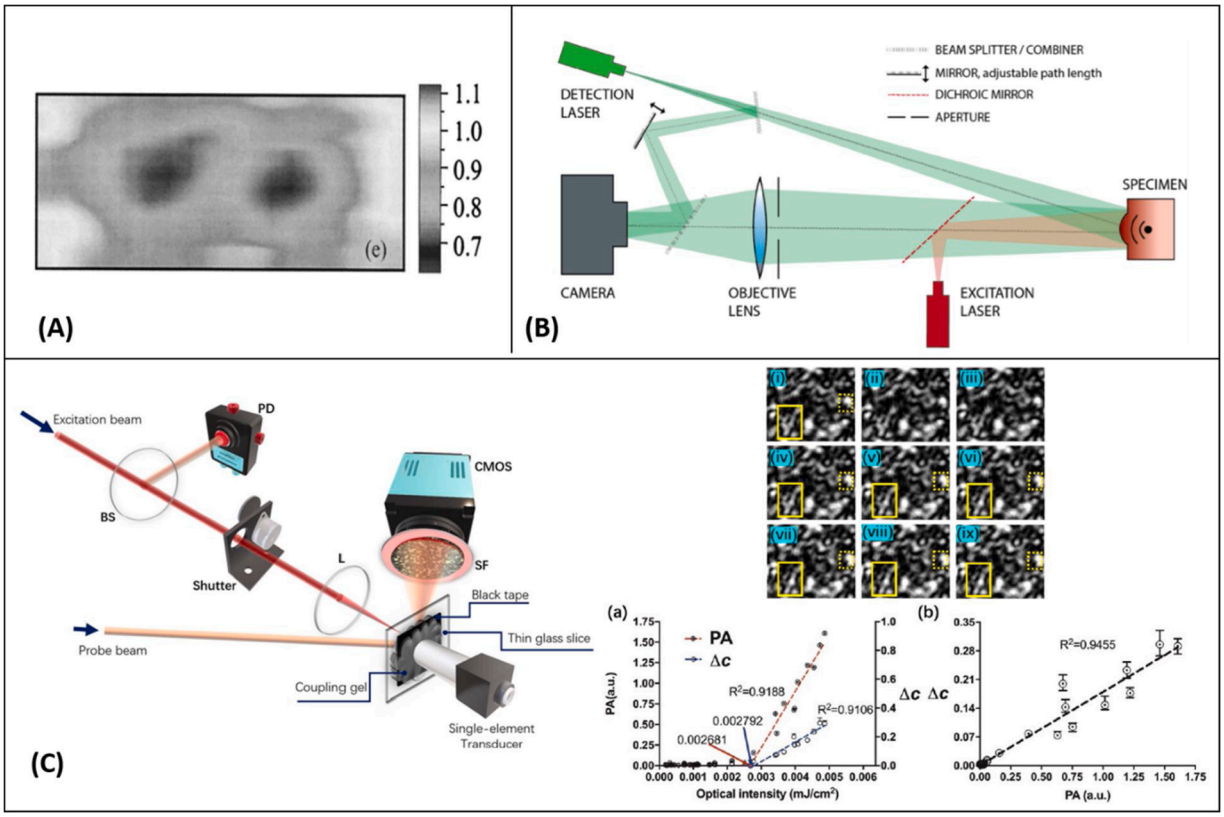


**Fig. 5.** **(A)** Two-dimensional image of chicken breast tissue in which two gizzard objects were buried, reprinted with permission from [153]. **(B)** Interferometric detection of object surface displacement after photoacoustic excitation. © Institute of Physics and Engineering in Medicine. Reproduced by permission of IOP Publishing [155]. All rights reserved. **(C)** Schematic setup for specklegram-based non-contact photoacoustic detection. BS, beamsplitter; CMOS, CMOS camera; L, lens; PD, photodiode; SF, spectral filter. Speckle pattern generated by the probe beam observed for various moments (i)–(ix) in (a). Among them, (i) is the initial speckle pattern, (ii) and (iii) are recorded when the shutter is off, and no excitation beam is illuminated on the sample, and (iv)–(ix) are a sequence of patterns associated with the excitation of PA effect. (a) Measured speckle correlation changes as a function of excitation pulse energy (right axis) and the ultrasound piezoelectric transducer-based PA amplitude as a function of excitation pulse energy (left axis). (b) Linearity between the two detection methods, reprinted with permission from [156].

reported a full-field speckle interferometry method where the back-scattered light was combined with a reference and imaged onto a high-speed camera. This experimental setup is demonstrated in Fig. 5B. Through consecutive measurements, they were able to extract signals from porcine skin phantoms with a 90 μm lateral resolution over a 4 mm penetration depth range. Lengenfelder et al. [144] performed experiments in both reflection and transmission modes for *ex-vivo* fat tissue imaging. To increase the SNR of the system, the optical exposure was 5-times higher than the ANSI MPE limits for biological tissues. They went on to further apply speckle pattern analysis for endoscopic applications and demonstrated 2.76 μm lateral resolution on phantoms and *ex-vivo* porcine fat tissue using a high frame rate camera (823,500 fps) [93]. Recently, Li et al. [156] evaluated the feasibility of delineating the strength of PA signals using a two-beam optical design and a CMOS camera operating at 60 Hz with a 10 $\mu s$ exposure. A black tape phantom was imaged and by correlating the speckle patterns as a function of time, the strength of PA perturbations was quantified (Fig. 5C). In the report, the probe beam was not focused at the sample interface resulting in a reflected speckle pattern that was highly sensitive to surface motion on the sample. As well, the bandwidth of the camera proved insufficient for capturing salient MHz-regime signals limiting its potential efficacy. However, this would need to be balanced against the resulting decrease in SNR brought on by lower integration times. Since any form of motion and mechanical noise can distort the speckle patterns of the probe beam, this method is very sensitive to phase noise and ambient motions and *in-vivo* applications would be extremely limited.

### 6.2.2. *Interferometric PA detection methods*

Interferometric approaches have become a popular method for remote detection of photoacoustic signals. They overcome some of the issues brought forward with speckle-based detection by leveraging dedicated interferometers for extraction of phase-contrast from light returning from the sample. Both homodyne and heterodyne architectures have been investigated for ultrasound signal detection [157,158]. In homodyne mode, interference occurs between beams of the same frequency, and the phase difference of the beams results in an intensity modulation of the detected light [159]. On the other hand, in heterodyne mode, the interference occurs between beams with different frequencies, generating an interference with one constant component and one oscillating component where the amplitude of the oscillating component is proportional to the product of the interfering beams [160–163]. In general, heterodyne interferometers are relatively less sensitive to ambient noise compared with homodyne variants [164]. Each of these methods depends on the tissue surface as well as the stability of the entire detection system, which will be discussed in the following sections.

*6.2.2.1. Heterodyne detection.* In 1968, Massey et al. [165] demonstrated the application of an optical heterodyne system for sensing the vibration amplitude distribution on a reflective resonant diaphragm placed in the liquid acoustic medium. The method was further applied for all-optical detection of PA signals in spectroscopy [166,167] and imaging applications [168,169]. In 2014, Park et al. [170] explored an all-fiber heterodyne interferometer for photoacoustic imaging. They

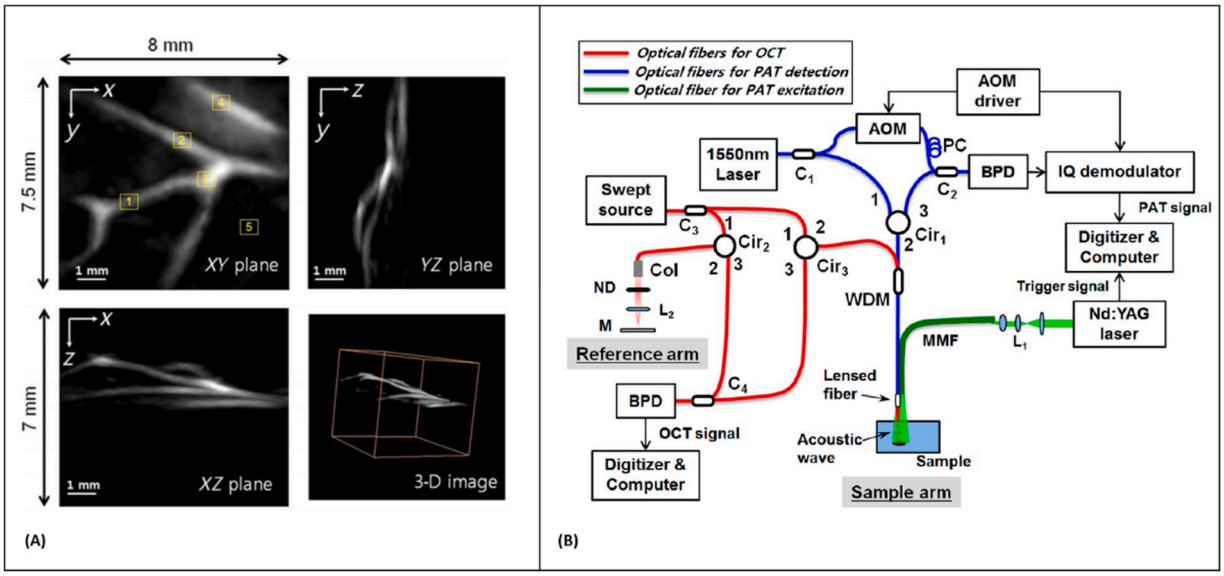


**Fig. 6.** **(A)** 3-D photoacoustic images of the CAM. Top left: XY plane maximum intensity projection (MIP) image. Top right: YZ plane MIP image. Lower left: XZ plane MIP image. Lower right: 3-D image, reprinted with permission from [168] **(B)** Schematic of all-fiber-based dual modality PA-OCT with miniature common probe. AOM: acousto-optic modulator; PC polarization controller, BPD: balanced photodetector, Col: collimator; ND: neutral density filter; WDM: Wavelength division multiplexer; MMF: multimode fiber, reprinted with permission from [171].

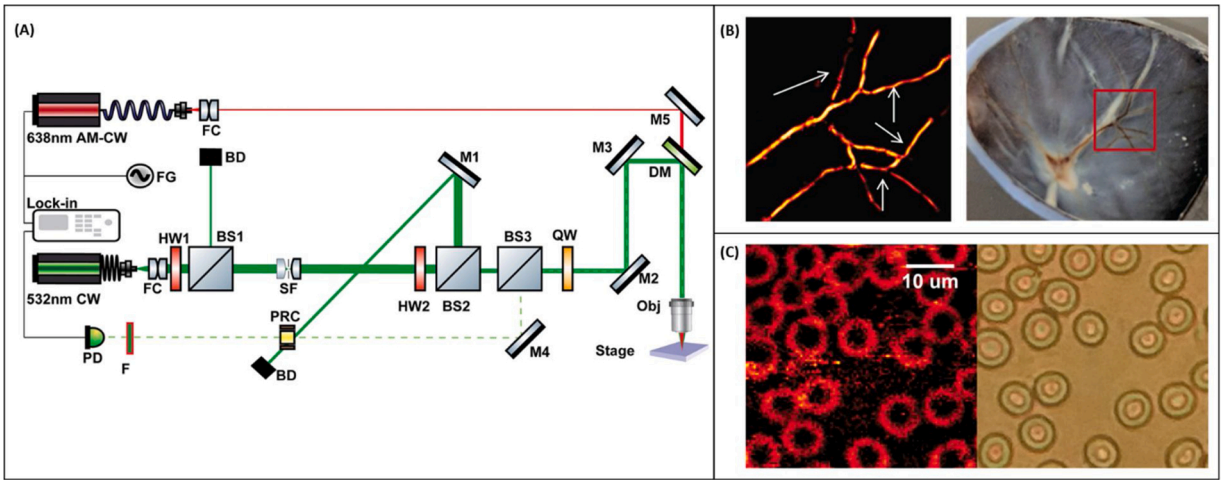


**Fig. 7.** **(A)** Schematic of the PRC-based PAM system. FC: fiber optic collimator, M: Mirror, DM: dichroic mirror, QW: quarter-waveplate, OBJ: objective, BS: beamsplitter, HW: half-waveplate PRC: photorefractive crystal, BD: beam dump, PD: photodetector, F: laser line filter. **(B)** (left) PAM image of *ex-vivo* retinal samples, (right) Photograph of the sample. **(C)** (left) photoacoustic image of blood smear showing RBC; (right) corresponding bright field image. Reprinted with permission from [181].

reported 1.7 μm lateral resolution from a miniaturized probe looking at polyethylene terephthalate fibers positioned inside the gelatin-based phantom. However, the excitation fluence used in this study was above ANSI MPE limits. The year after, Eom et al. [168] reported a different fiber-optic heterodyne interferometer looking at a chicken chorioallantois membrane (CAM). Blood vessel structures as deep as 2.5 mm were identified with lateral and axial resolutions of 100 μm and 30 μm, respectively (Fig. 6A). They further developed the system into a dual-modality imaging technique by integrating the photoacoustic detection with a swept-source optical coherence tomography (OCT) for endoscopic imaging (Fig. 6B) [171]. Acoustic waves were detected at the outer surface of the water layer under which the sample was submerged. The method was also applied for non-contact delineation of stereotactic boundaries of artificial tumor in pig brain tissue and was successful in providing accurate thickness information of the sample [172].

Heterodyne interferometers have difficulty detecting highly scattered probe beams on rough surfaces, and therefore require a thin layer of water or oil above the sample [168,172]. This provides an appropriate smooth and reflective surface for the interferometer; however, the method can no longer be considered fully non-contact (called quasi non-contact) as the system requires the addition of fluid to the surface of the sample. Much like standard acoustic coupling performed in conventional PAI techniques, this greatly limits potential biomedical applications.

A solution that was explored involved the application of a two-wave-mixing interferometer (TWMI) [173,174]. In these devices the beams interfere inside a photorefractive nonlinear crystal, where the beams are amplified and low frequency noises are suppressed so the effect of ambient noises like air disturbance is negligible [175,176]. While the technique is mainly used for non-destructive testing applications [177], biomedical applications like skin imaging have also been explored [178–180].

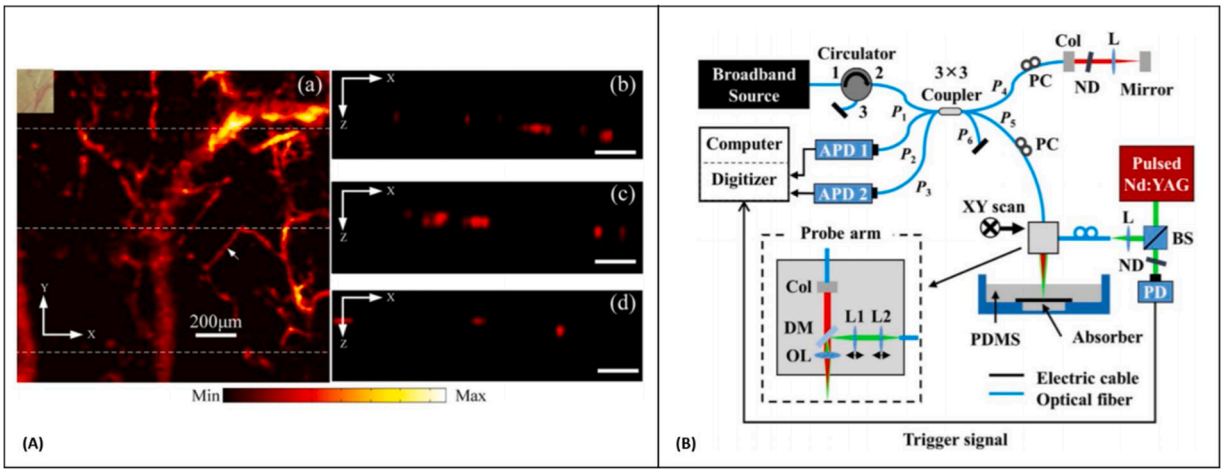


**Fig. 8.** **(A)** In vivo photoacoustic image of microvasculature of a mouse ear. (a) Photoacoustic maximum intensity projection of the microvasculature of a mouse ear. The total time for obtaining the photoacoustic image is 16.7 min. Inset: photograph of the imaging area. (b)–(d) B-scan image of microvasculature corresponding to the three white dotted line in (a) Reprinted from [185], with the permission of AIP Publishing **(B)** Schematic of the experimental setup. The probe beam and the excitation beam are combined and scanned together. APD, avalanche photodetector; ND, neutral density filter; Col, collimator; BS, beam splitter; DM, dichroic mirror; L, lens; OL, objective lens; P, fiber-optic coupler port; PC, polarization controller; PD, photodetector, Reprinted with permission from [187].

George et al. [181] developed a non-contact photoacoustic microscope utilizing a photorefractive crystal-based interferometer for imaging of red blood cells and *ex-vivo* porcine retinal samples. The schematic diagram of the system and representative images recorded with the system are presented in Fig. 7A CW laser with a wavelength of 532 nm operates as the light source for the interferometer, and the sample was irradiated using a diode laser operating at 638 nm. The reference and sample beam were combined inside the $Bi_{12}SiO_{20}$ crystal operating at its drift regime, leading to the formation of a dynamic hologram detected by the photodetector. The resolution of the microscope was estimated to be ~ 5.3 μm. Despite offering a completely non-contact detection scheme for imaging rough tissue surfaces, the excitation exposure was 3 times higher than the safe limit for skin imaging which may impede its application to *in-vivo* studies.

*6.2.2.2. Homodyne detection.* Depending on the coherence length of the light source used, homodyne interferometers employed for PA detection, can be divided into low-coherence and long-coherence. When a single beam of light is split and interfered with itself, coherent edition will only occur for path lengths which are less than the characteristic coherence length of the source. For low-coherence light sources this is generally on the order of microns, whereas it can reach kilometers for a long-coherence source. Techniques which use low-coherence interferometers generally leverage this low coherence as a means of path length discrimination since the absolute length of a sample path can be determined against a reference path of known length down to single-micron scales.

*6.2.2.2.1. Low-coherence devices. For* these devices interference only occurs for path lengths on the scale of the coherence length. This effect can be leveraged to omit scattered signals arising from depths which are far away from the reference path length. The coherence length of typical light sources used in a low-coherence interferometer is on the order of micrometers, and when compared to nanometer scale photoacoustic induced surface displacement, the coherence length of the source is larger by three orders of magnitude. For such small displacements the sensitivity of the interferometer depends on the initial phase of the system. Since an interference signal varies in a sinusoidal form, the highest sensitivity occurs when the initial phase is at the quadrature-point ($k\pi \pm \pi/2$) of the interferometer. However, it is difficult to maintain the quadrature-point consistently during the whole measurement period, as the system is sensitive to environmental perturbations such as vibration, and room temperature variation. To overcome this problem, feedback methods are introduced, in which the optical phase of an interferometric signal is adjusted using a motorized stage [182] or by changing the laser wavelength [183]. These feedback methods may slow down the imaging speed or invoke other external perturbations due to the mechanical movement of the stage. Wang et al. [184] developed a synchronization detection method, in which only measurements made at quadrature points were analyzed. The system was used for *in-vivo* imaging of blood vessels within the mouse ear. The PA signals were detected in quasi non-contact approach from the oil layer on top of the sample; and the system's axial and lateral resolutions were measured as 60 μm and 30 μm, respectively. The imaging speed was highly limited by the 10 Hz pulse repetition rate of the excitation source, slow scanning mirror in the detection interferometer, and the synchronization system. Chen et al. [185] reported a PAM system using an all-fiber low-coherence interferometer. The imaging speed of the system was improved by a piezoelectric actuator driving the reference mirror of the interferometer. The imaging time of collecting one dataset was ~17 min which was much faster than the 10 h imaging time reported by Wang et al. [184]. *In-vivo* images of mouse ear microvasculature with 11 μm lateral and ~ 20 μm axial resolution was demonstrated in quasi non-contact mode (Fig. 8A). A similar system was developed by Liu et al. [186] for PAT. The interferometer had a central wavelength at ~1300 nm and a spectral bandwidth of 46 nm; an axial and lateral resolution of 45 μm and ~15 μm was achieved, respectively for *in-vivo* imaging of mouse ear vasculature. Recently, Park et al. [187] employed the intrinsic phase difference of a multiport ($3 \times 3$) interferometer to reconstruct the photoacoustic signal without suffering from the initial phase drift (Fig. 8B). The performance of the system was evaluated by imaging human hairs embedded in polydimethylsiloxane resin block, and isometric resolution of ~ 85 μm over 1.5 mm imaging depth was reported. Generally, in an ideal $3 \times 3$ coupler, the return ports have an intrinsic phase difference of 120° to each other. Therefore, the quadrature component of the signal measured at one particular return port can be calculated using the measured signal at any other return port of the same coupler [188]. Moreover, the long-term variation of intrinsic phase difference in a $3 \times 3$ fiber-optic coupler is rather stable; and in it has slight effect on the displacement measurement [189]. The proposed system eliminated the need for any feedback components. However, the imaging speed was again highly limited by the low repetition rate of the excitation laser which prevented *in-vivo* experiments. In general, for a low-coherence interferometer the sensitivity decreases when the optical path difference (OPD) between two arms increases, and it turns to zero

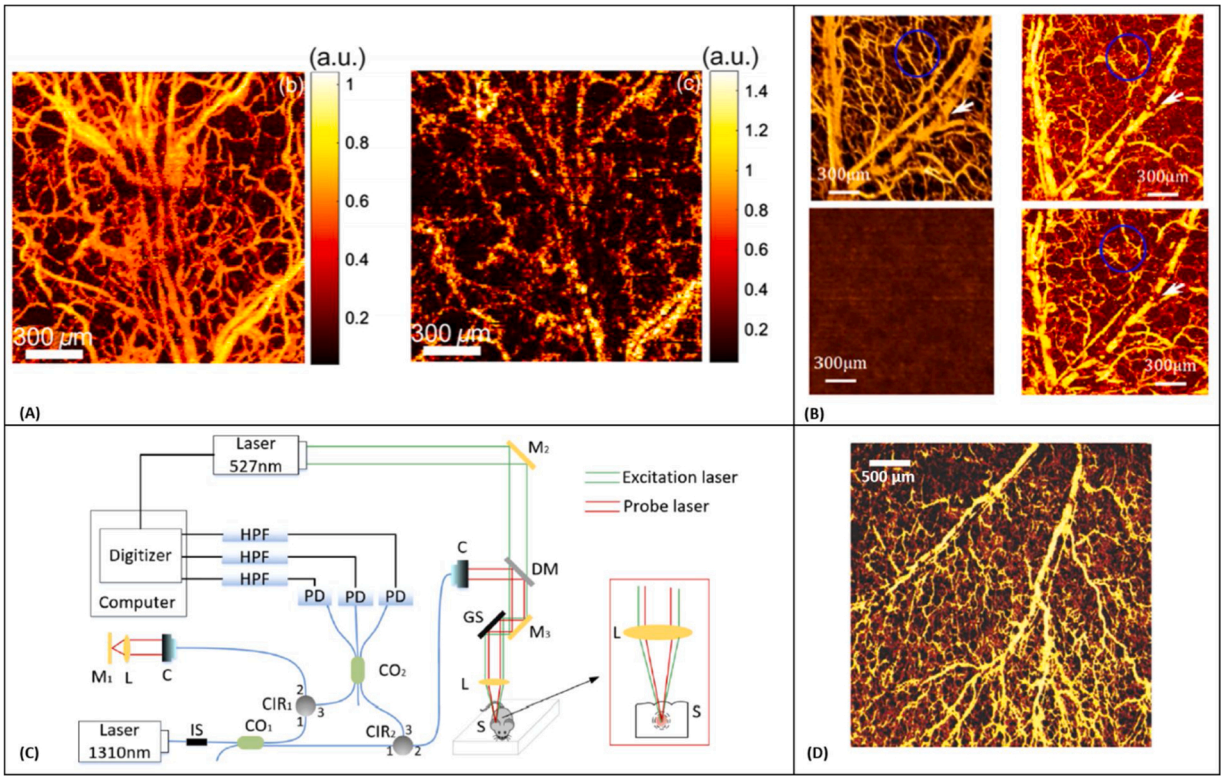


**Fig. 9.** **(A)** In vivo photoacoustic images of blood vessels in the mouse ear (left) with and (right) without water layer on top, Reprinted with permission from [191]. **(B)** differentiation of blood flow states with the dual-modal system. (left) En-face microvasculature image of OCT angiography, (right) photoacoustic image of mouse pinna, (top) images with blood flow, (down) images with blood flow blocked, Reprinted with permission from [190]. (C) Schematic of the multiport photoacoustic imaging system. Reprinted with permission from [192] (D) Photoacoustic MAP image acquired *in-vivo* from mouse ear. Reprinted with permission from [192].

when the OPD is greater than the coherence length of the light source [190]. This might not be an issue for imaging thin samples like mouse ear and ex-vivo studies. However, while imaging thick samples or *in-vivo* experiments where motion is unavoidable, it would become a severe issue.

*6.2.2.2.2. Long-coherence devices.* To overcome the sensitivity dependence of low-coherence interferometers and to maintain constant sensitivity over a large dynamic range of OPDs, long-coherence interferometers can be used. Lu et al. [191] utilized a homodyne interferometer with ~ 17 mm coherence length along with a synchronization method to lock the system at its maximum sensitivity. The imaging was performed in quasi non-contact mode using a water layer on top the mouse ear, demonstrating *in-vivo* images of blood vessels. Images with and without a water layer on top of the sample are shown in Fig. 9A. It is clear that the water layer on the sample surface plays a crucial role in the method. Ma et al. [190] utilized a similar technology and developed a dual-modality imaging system combining spectral-domain OCT with PAM. The system was utilized for *in-vivo* blood flow assessment in mouse ear. In the PAI subsystem, surface vibrations of the water layer on top of the sample were detected by a homodyne interferometer operating at 1310 nm with a 0.1 nm bandwidth. The vasculature in the mouse ear were imaged with normal and impeded blood circulations. The experimental results indicated that the integrated system could differentiate blood flow states and improved visualization of conditions such as hemorrhage (Fig. 9B). Wang et al. [192] recently employed a multiport ($3 \times 3$) fiber coupler homodyne interferometer centered at 1310 nm with a coherence length of more than several hundred millimeters (Fig. 9C). The multiport interferometer eliminated the influence of initial phase and the phase perturbation from the environment. The intensity changes of the probe beam were used to reconstruct the photoacoustic images. The method offered several advantages including, freedom from the influence of the rough tissue surface and having a confocal configuration to focus both probe light and excitation light at a common point below the sample surface. The system demonstrated *in-vivo* imaging of the blood vessels of a mouse ear with an excitation fluence well within the ANSI MPE limits (Fig. 9D). In general, long coherence devices may suffer from unwanted interferences due to reflection from the optical components and sample structures.

The interferometric detection of photoacoustic signals has several significant technical limitations. First, the rough tissue surface dramatically affects the quality of the image when directly measuring the vibration of the tissue surface. This motivates the use of a water/oil layer on the surface of the sample. Secondly, in most of these methods except the one proposed by Wang et al. [192], the probe beam is focused on the surface of the sample or water layer, while the excitation beam was focused below the surface. This requires elaborate adjustment of the probe beam, making it difficult to perform *in-vivo* imaging due to the uneven surface of the tissue and motion of the sample. Finally, to maintain the interferometric system at its highest sensitivity, complicated phase stabilization techniques are required, which sacrifice the imaging speed, and limited success could be achieved in well-controlled lab settings [193].

### 6.2.3. Non-interferometric photoacoustic remote sensing (PARS)

Photoacoustic remote sensing (PARS) microscopy was first introduced by HajiReza et al. [194] in 2017, for non-contact non-interferometric detection of photoacoustic signals. In PARS microscopy, a nanosecond excitation beam is co-focused with a continuous-wave probe beam into the target. The absorbed optical energy from the excitation pulse is converted to pressure through thermo-elastic expansion. This pressure rise produces elasto-optic modulations within the absorber, changing the intensity of the back-reflected probe beam. The magnitude of these optical signals is proportional to the optical absorption of the excitation wavelength. The confocal detection scheme

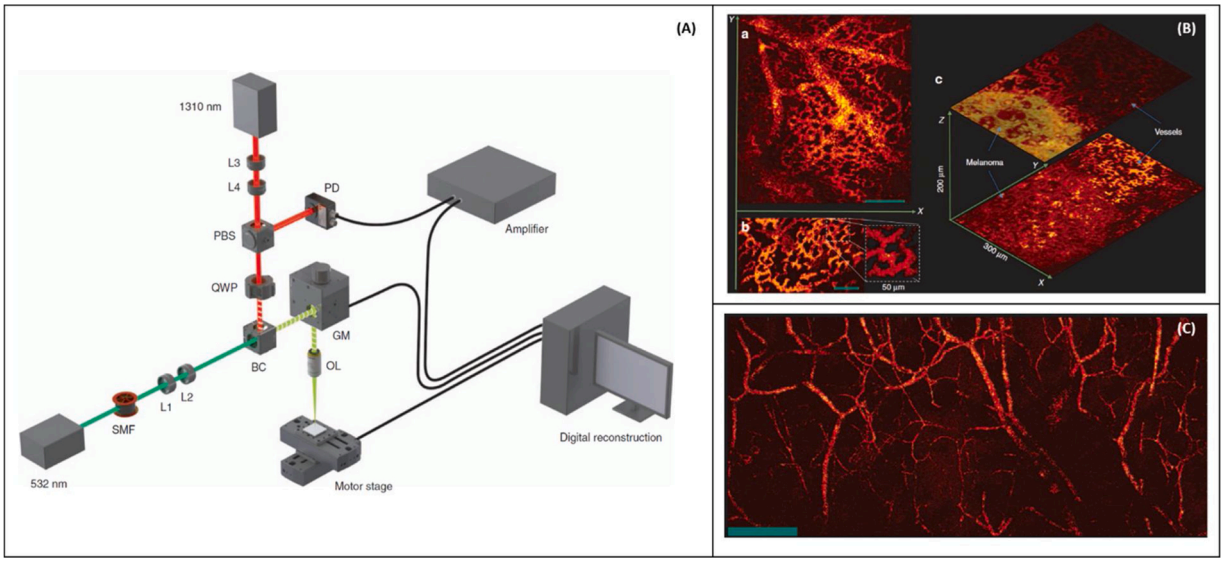


**Fig. 10.** **(A)** Experimental setup. PARS microscopy, **(B)** *in-vivo* images of a chicken embryo. (**a**) En-face C-scan PARS images (**b**) A snapshot of real-time imaging of capillaries (**c**) PARS images of a melanoma tumor and surrounding vasculature. Scale bar: 100 µm (C) *in vivo* en-face mouse ear images. (a) PARS images using two-axis lateral mechanical scanning. (b) Larger field of view images using mechanical scanning as well as a zoomed in image of both capillary beds and larger blood vessels. Scale bar: 500 µm. PBS: polarized beamsplitter, QWP: quarter-waveplate, BC: beam combiner, PD: photodiode, GM: galvo-scanner mirrors, SMF: single mode fiber, OL: objective lens, L: lens. Reprinted with permission from [189].

enables detection of the photoacoustic signal at the subsurface origin where the pressure is maximum. Moreover, by intentionally rejecting phase information, it exclusively monitors back-reflected intensity changes. Schematic of the proposed experimental setup is illustrated in Fig. 10A, and *in-vivo* images and snapshots recorded from capillaries and melanoma tumor are shown in Fig. 10B. The reported excitation beam surface fluence for *in-vivo* imaging was $\sim 0.5\ mJ/cm^2$ which is about 12 times lower than the ANSI limits, similarly the surface average power of the interrogation beam was 0.4 $W/cm^2$ which is about 8 times lower than ANSI safety limits. Large field-of-view *in-vivo* images acquired from the mouse ear with $\sim 2.7$ µm lateral resolution are presented in Fig. 10C.

PARS has also demonstrated deep non-contact imaging at depths beyond the optical transport mean-free path of the excitation wavelength by leveraging a pseudo-AR-PAM imaging mode where a short-wave infrared (SWIR) detection beam provides lateral resolution [195]. In this study, the excitation beam spot size on the sample was $\sim 30$ times larger than the SWIR interrogation beam, therefore the optical resolution was maintained solely by the focused probe beam. Experimental results demonstrated optical resolution to depths of 2.5 mm in tissue-mimicking scattering media. Images acquired *in-vivo* from single red blood cells, oxygen saturation mapping, and deep-vasculatures are presented in Fig. 11. Oxygen saturation measurement was achieved by utilizing spectra generated using stimulated Raman scattering (SRS) in a single mode fiber. Additionally, a fully fiber-tetherable design of the system for real-time functional imaging was reported, and characterized by estimating blood oxygen saturation in blood-flow phantoms and with *in*-vivo mouse ear microvasculature [196].

Recently, Abbasi et al. [197–199] utilized the UV absorption peak of DNA to visualize cell nuclei and bulk tissue structure. Human breast tissue with invasive ductal carcinoma was imaged in their study and showed good agreement with the cellular morphology in the H&E samples. Representative image mosaic of one hundred frames, with each frame being 85 µm × 85 µm and consisting of 100,000 points is presented in Fig. 12.

PARS techniques read out phase-independent intensity data, and time-resolved signals do not produce depth-resolved information, therefore volume scanning must be done by optical sectioning. Bell et al. [200] proposed an approach for providing coherence-gated depth-resolved images utilizing the difference between pulsed-interrogation OCT scan-lines with and without excitation pulse and validated the method using simulations, however, the experimental results have yet to be investigated.

## 7. Summary

Photoacoustic imaging offers a hybrid *in-vivo* imaging technique that detects optical contrast via the photoacoustic effect. Photoacoustic microscopy is usually categorized with all-optical microscopy techniques such as optical coherence tomography or confocal microscopes. Unlike these pure optical microscopes, PAM can break through the optical diffusion limit and provide high resolution images at imaging depths up to a few millimeters [201]. Compared to backscattering-based optical coherence tomography and confocal microscopy that provide scattering contrast, PAM techniques offer direct optical absorption contrast. Additionally, PAM instruments are usually label-free techniques which can image more molecules at their absorption wavelengths than fluorescence-based microscopy methods. Furthermore, using endogenous and exogenous contrast agents, PAM techniques are capable to provide anatomical, functional, molecular, flow dynamic and metabolic contrasts simultaneously. Photoacoustic microscopes have the potential to be combined with other imaging modalities to provide complementary imaging contrasts and offer a direction for future microscopes development [202–205].

Despite offering high sensitivity, novel imaging contrast, and high resolution, PAM is not generally an all-optical imaging method unlike the other microscopy techniques. One of the significant limitations of photoacoustic microscopes arises from their need to be in physical contact with the sample through a coupling media. This physical contact, coupling, or immersion of the sample is undesirable or impractical for many clinical and pre-clinical applications.

The recent advancements in all-optical photoacoustic microscopes has led to significant progress of PA instruments applied for various biomedical applications. Due to the high ultrasound detection sensitivity, uniform amplitude response over a wide frequency range, miniaturized size, and their optical transparency, optical detection methods are ideally suited for high-resolution photoacoustic imaging applications [206–209]. Several experiments have demonstrated the capability of all-optical detection methods for non-contact detection of ultrasound

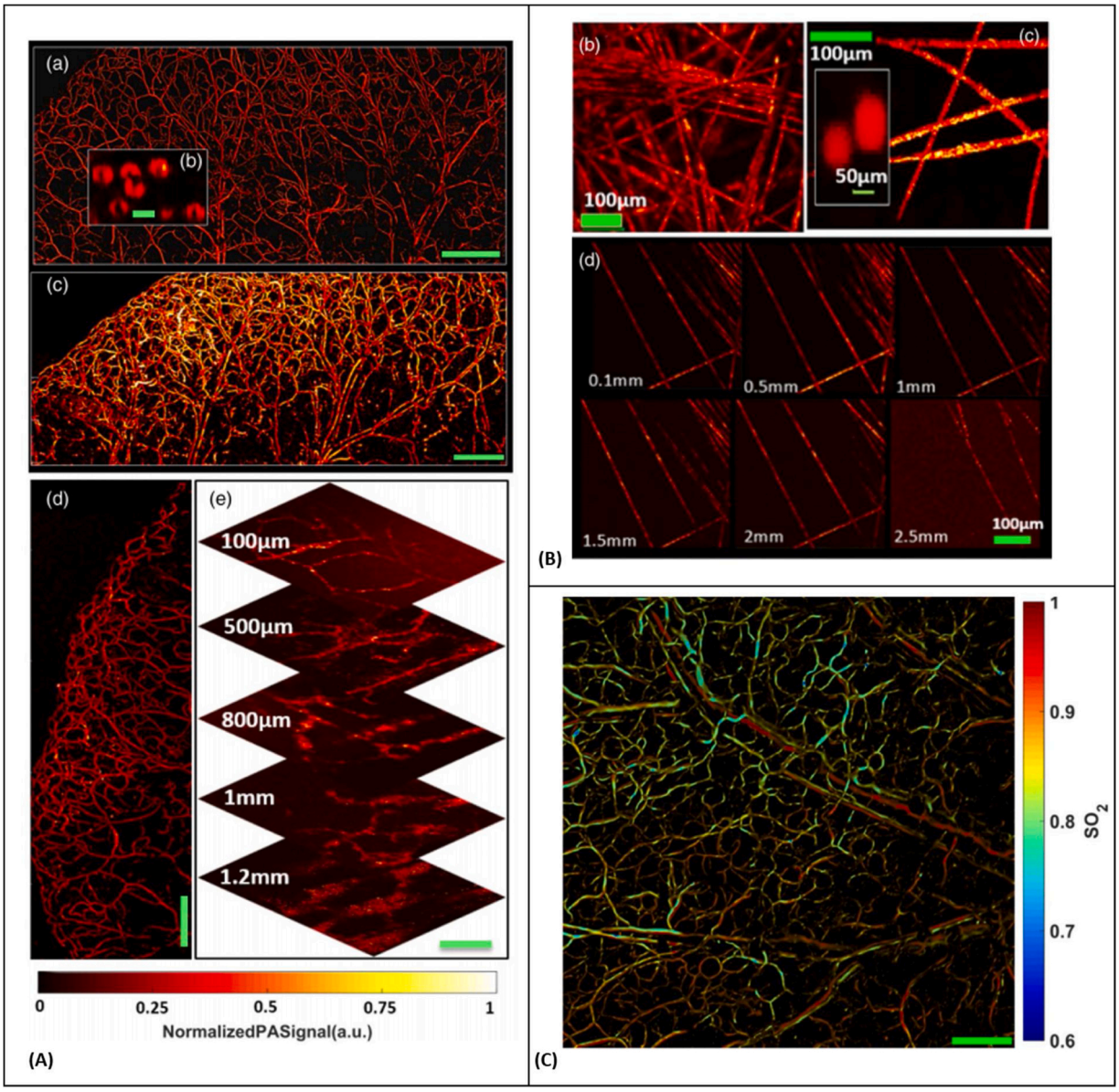


**Fig. 11.** **(A)** In vivo PARS microscopy structural images. (a) Image of en face microvasculature in mouse ear using the high-resolution mode (Scale bar: 500 µm) (b) *In-vivo* image of red blood cells in the mouse ear using the high-resolution mode (Scale bar: 5 µm) (c) Image of mouse ear vasculature using the deep-penetrating mode (Scale bar: 500 µm) (d) Image of en face microvasculature in the tip of a mouse ear using the high-resolution mode (Scale bar: 500 µm) (e) Images of back flank of mouse at various depths using the deep penetrating mode (Scale bar: 100 µm) **(B)** Image of carbon fiber networks using the deep penetrating imaging mode. (c) Image of carbon fiber networks using the high-resolution imaging mode, as well as an inset image of 100-nm gold nanoparticles. (d) Images of carbon fiber networks at various depths in tissue-mimicking solution. **(C)** Functional images SO2 measurement of en face microvasculature in the ear of an 8-week-old nude mouse. Reprinted with permission from [195].

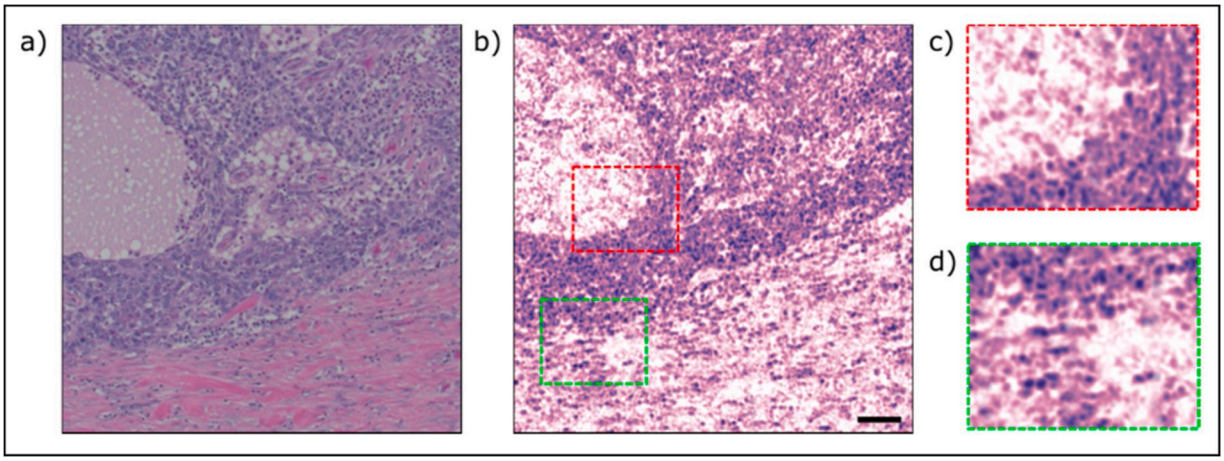


**Fig. 12.** A comparison between a PARS image of unstained human breast tissue with conventional bright-field microscope. (a) a standard H&E stained image (b) a PARS mosaic of one hundred frames, total field of view of 1 mm × 1 mm (c,d) zoomed in versions of (b) showing cell nuclei. The image was acquired with a 266 nm excitation source operating at 20 kHz. Scale bar 100 μm. Reprinted with permission from [198].

signals. While non-contact detection of PA signal could offer advantages for biomedical imaging applications, there are still challenges to be overcome in terms of detection sensitivity and sample exposure. Novel all-optical PAM systems can be investigated in terms of sensitivity, penetration depth, temporal and spatial resolutions in coming years. They have the potential to be transfer from bench to bedside and are expected to find applications in preclinical and clinical practices, including but not limited to endoscopic applications, cancer detection and histology-like imaging, ophthalmic imaging, tumor angiogenesis, drug delivery and brain metabolism.

## Declaration of Competing Interest

Authors K. Bell, and P. Haji Reza have financial interests in illumiSonics Inc. IllumiSonics partially supported this work.

## Acknowledgements

The authors acknowledge funding from the University of Waterloo, NSERC Discovery grant, MITACS accelerator program, Canada Foundation for Innovation (CFI-JEFL), Centre for Bioengineering and Biotechnology seed funding, New Frontiers in Research Fund – exploration, and research partnership support from illumiSonics Inc.

## References

[1] A.G. Bell, On the production and reproduction of sound by light, Proc. Am. Assoc. Adv. Sci. 29 (1881) 115–136.
[2] L. Amar, Detection d'omes elastiques (ultrasonores) sur l'os occipital, induites par impulsions laser dans l'oeil d'un lapin, CR Acad. Sc. Paris 259 (1964) 3653–3655.
[3] L. Amar, M. Bruma, M. Velghe, P. Desvignes, On the detection of laser induced ultrasonic waves in the human eye and the elaboration of a theory on the fundamental mechanism of vision, Z. Für Angew. Math. Phys. ZAMP 16 (1) (1965) 182–183.
[4] T. Bowen, Radiation-induced thermoacoustic soft tissue imaging, 1981 Ultrasonics Symposium (1981) 817–822, https://doi.org/10.1109/ULTSYM.1981.197737.
[5] Q.X. Chen, A. Davies, R.J. Dewhurst, P.A. Payne, Photo-acoustic probe for intra-arterial imaging and therapy, Electron. Lett. 29 (18) (1993) 1632–1633, https://doi.org/10.1049/el:19931087. Sep.
[6] P. Hajireza, A. Forbrich, R. Zemp, In-Vivo functional optical-resolution photoacoustic microscopy with stimulated Raman scattering fiber-laser source, Biomed. Opt. Express 5 (2) (2014) 539, https://doi.org/10.1364/BOE.5.000539. Feb.
[7] J. Yao, et al., High-speed label-free functional photoacoustic microscopy of mouse brain in action, Nat. Methods 12 (5) (2015) 407–410, https://doi.org/10.1038/nmeth.3336. May.
[8] C.L. Bayer, G.P. Luke, S.Y. Emelianov, Photoacoustic imaging for medical diagnostics, Acoust. Today 8 (4) (2012) 15, https://doi.org/10.1121/1.4788648.
[9] E.W. Stein, K.I. Maslov, L.V. Wang, Noninvasive, in vivo imaging of blood-oxygenation dynamics within the mouse brain using photoacoustic microscopy, J. Biomed. Opt. 14 (2) (2009) 020502.
[10] J. Laufer, E. Zhang, G. Raivich, P. Beard, Three-dimensional noninvasive imaging of the vasculature in the mouse brain using a high resolution photoacoustic scanner, Appl. Opt. 48 (10) (2009) D299–D306.
[11] V. Tsytsarev, K.I. Maslov, J. Yao, A.R. Parameswar, A.V. Demchenko, L.V. Wang, In vivo imaging of epileptic activity using 2-NBDG, a fluorescent deoxyglucose analog, J. Neurosci. Methods 203 (1) (2012) 136–140.
[12] R.J. Paproski, A. Heinmiller, K. Wachowicz, R.J. Zemp, Multi-wavelength photoacoustic imaging of inducible tyrosinase reporter gene expression in xenograft tumors, Sci. Rep. 4 (2014) 5329.
[13] S. Sethuraman, J.H. Amirian, S.H. Litovsky, R.W. Smalling, S.Y. Emelianov, Ex vivo characterization of atherosclerosis using intravascular photoacoustic imaging, Opt. Express 15 (25) (2007) 16657, https://doi.org/10.1364/OE.15.016657.
[14] J.-T. Oh, M.-L. Li, H.F. Zhang, K. Maslov, L.V. Wang, Three-dimensional imaging of skin melanoma in vivo by dual-wavelength photoacoustic microscopy, J. Biomed. Opt. 11 (3) (2006) 034032.
[15] T.T. Wong, et al., Fast label-free multilayered histology-like imaging of human breast cancer by photoacoustic microscopy, Sci. Adv. 3 (5) (2017) e1602168.
[16] S.M. Maswadi, et al., All-optical optoacoustic microscopy based on probe beam deflection technique, Photoacoustics 4 (3) (2016) 91–101.
[17] R. Lin, J. Chen, H. Wang, M. Yan, W. Zheng, L. Song, Longitudinal label-free optical-resolution photoacoustic microscopy of tumor angiogenesis in vivo, Quant. Imaging Med. Surg. 5 (1) (2015) 23–29, https://doi.org/10.3978/j.issn.2223-4292.2014.11.08. Feb.
[18] L. Li, et al., Small near-infrared photochromic protein for photoacoustic multi-contrast imaging and detection of protein interactions in vivo, Nat. Commun. 9 (1) (2018), https://doi.org/10.1038/s41467-018-05231-3. Art. no. 1, Jul.
[19] M.R. Kelly-Goss, et al., Dynamic, heterogeneous endothelial Tie2 expression and capillary blood flow during microvascular remodeling, Sci. Rep. 7 (1) (2017) 9049, https://doi.org/10.1038/s41598-017-08982-z. Dec.
[20] S. Jeon, et al., In vivo photoacoustic imaging of anterior ocular vasculature: a random sample consensus approach, Sci. Rep. 7 (1) (2017) 4318, https://doi.org/10.1038/s41598-017-04334-z. Dec.
[21] C. Tian, W. Zhang, V.P. Nguyen, X. Wang, Z. Huang, Y.M. Paulus, Integrated photoacoustic microscopy, optical coherence tomography, and fluorescence microscopy for multimodal chorioretinal imaging. Photons Plus Ultrasound: Imaging and Sensing 2018, San Francisco, United States, Feb., 2018, p. 204, https://doi.org/10.1117/12.2290594.
[22] V. Nguyen, Y. Paulus, Photoacoustic ophthalmoscopy: principle, application, and future directions, J. Imaging 4 (12) (2018) 149, https://doi.org/10.3390/jimaging4120149. Dec.
[23] X. Cai, B.S. Paratala, S. Hu, B. Sitharaman, L.V. Wang, Multiscale photoacoustic microscopy of single-walled carbon nanotube-incorporated tissue engineering scaffolds, Tissue Eng. Part C Methods 18 (4) (2012) 310–317, https://doi.org/10.1089/ten.tec.2011.0519. Apr.
[24] S.Y. Nam, L.M. Ricles, L.J. Suggs, S.Y. Emelianov, In vivo ultrasound and photoacoustic monitoring of mesenchymal stem cells labeled with gold nanotracers, PLoS One 7 (5) (2012) e37267, https://doi.org/10.1371/journal.pone.0037267. May.
[25] L. Yan, C. Gao, B. Zhao, X. Ma, N. Zhuang, H. Duan, Non-destructive imaging of standard cracks of railway by photoacoustic piezoelectric technology, Int. J. Thermophys. 33 (10) (2012) 2001–2005, https://doi.org/10.1007/s10765-012-1253-6. Nov.
[26] M. Sun, X. Lin, Z. Wu, Y. Liu, Y. Shen, N. Feng, Non-destructive photoacoustic detecting method for high-speed rail surface defects, in: 2014 IEEE International

Instrumentation and Measurement Technology Conference (I2MTC) Proceedings, May, 2014, pp. 896–900, https://doi.org/10.1109/I2MTC.2014.6860871.
[27] S. Jeon, J. Kim, J.P. Yun, C. Kim, Non-destructive photoacoustic imaging of metal surface defects, J. Opt. 18 (11) (2016) 114001, https://doi.org/10.1088/2040-8978/18/11/114001. Nov.
[28] H. Wu, et al., Beat frequency quartz-enhanced photoacoustic spectroscopy for fast and calibration-free continuous trace-gas monitoring, Nat. Commun. 8 (1) (2017), https://doi.org/10.1038/ncomms15331. Art. no. 1, May.
[29] P. Patimisco, G. Scamarcio, F.K. Tittel, V. Spagnolo, Quartz-enhanced photoacoustic spectroscopy: a review, Sensors 14 (4) (2014), https://doi.org/10.3390/s140406165. Art. no. 4, Apr.
[30] G.J. Tserevelakis, et al., Photoacoustic imaging reveals hidden underdrawings in paintings, Sci. Rep. 7 (1) (2017) 747, https://doi.org/10.1038/s41598-017-00873-7. Dec.
[31] L.V. Wang, H.-I. Wu, Biomedical Optics: Principles and Imaging, John Wiley & Sons, Inc., Hoboken, NJ, USA, 2009.
[32] L.V. Wang, H. Wu, Biomedical Optics: Principles and Imaging, John Wiley & Sons, 2012.
[33] M. Xu, L.V. Wang, Photoacoustic imaging in biomedicine, Rev. Sci. Instrum. 77 (4) (2006) 041101, https://doi.org/10.1063/1.2195024. Apr.
[34] D.-K. Yao, C. Zhang, K.I. Maslov, L.V. Wang, Photoacoustic measurement of the Grüneisen parameter of tissue, J. Biomed. Opt. 19 (1) (2014) 017007.
[35] E. Petrova, S. Ermilov, R. Su, V. Nadvoretskiy, A. Conjusteau, A. Oraevsky, Using optoacoustic imaging for measuring the temperature dependence of Grüneisen parameter in optically absorbing solutions, Opt. Express 21 (21) (2013) 25077, https://doi.org/10.1364/OE.21.025077. Oct.
[36] J. Yao, L.V. Wang, Sensitivity of photoacoustic microscopy, Photoacoustics 2 (2) (2014) 87–101.
[37] J. Chan, Z. Zheng, K. Bell, M. Le, P.H. Reza, J.T. Yeow, Photoacoustic imaging with capacitive micromachined ultrasound transducers: principles and developments, Sensors 19 (16) (2019) 3617.
[38] L.V. Wang, Tutorial on photoacoustic microscopy and computed tomography, IEEE J. Sel. Top. Quantum Electron. 14 (1) (2008) 171–179.
[39] J. Xia, et al., Whole-body ring-shaped confocal photoacoustic computed tomography of small animals in vivo, J. Biomed. Opt. 17 (5) (2012) 050506.
[40] L.V. Wang, S. Hu, Photoacoustic tomography: in vivo imaging from organelles to organs, science 335 (6075) (2012) 1458–1462.
[41] Y. Liu, L. Nie, X. Chen, Photoacoustic molecular imaging: from multiscale biomedical applications towards early-stage theranostics, Trends Biotechnol. 34 (5) (2016) 420–433, https://doi.org/10.1016/j.tibtech.2016.02.001. May.
[42] J. Xia, C. Huang, K. Maslov, M.A. Anastasio, L.V. Wang, Enhancement of photoacoustic tomography by ultrasonic computed tomography based on optical excitation of elements of a full-ring transducer array, Opt. Lett. 38 (16) (2013) 3140–3143, https://doi.org/10.1364/OL.38.003140. Aug.
[43] H.-P. Brecht, R. Su, M. Fronheiser, S.A. Ermilov, A. Conjusteau, A.A. Oraevsky, Whole-body three-dimensional optoacoustic tomography system for small animals, J. Biomed. Opt. 14 (6) (2009) 064007, https://doi.org/10.1117/1.3259361.
[44] J.K. Gamelin, et al., Curved array photoacoustic tomographic system for small animal imaging, J. Biomed. Opt. 13 (2) (2008) 024007, https://doi.org/10.1117/1.2907157. Mar.
[45] J. Yao, et al., Noninvasive photoacoustic computed tomography of mouse brain metabolism in vivo, NeuroImage 64 (2013) 257–266, https://doi.org/10.1016/j.neuroimage.2012.08.054. Jan.
[46] M. Toi, et al., Visualization of tumor-related blood vessels in human breast by photoacoustic imaging system with a hemispherical detector array, Sci. Rep. 7 (1) (2017), https://doi.org/10.1038/srep41970. Art. no. 1, Feb.
[47] J. Xia, J. Yao, L.V. Wang, Photoacoustic tomography: principles and advances, Electromagn. Waves Camb. Mass 147 (2014) 1.
[48] L.V. Wang, J. Yao, A practical guide to photoacoustic tomography in the life sciences, Nat. Methods 13 (8) (2016) 627–638, https://doi.org/10.1038/nmeth.3925. Aug.
[49] J. Xia, et al., Whole-body ring-shaped confocal photoacoustic computed tomography of small animals in vivo, J. Biomed. Opt. 17 (5) (2012) 050506, https://doi.org/10.1117/1.JBO.17.5.050506.
[50] L. Lin, et al., Single-breath-hold photoacoustic computed tomography of the breast, Nat. Commun. 9 (1) (2018) 2352, https://doi.org/10.1038/s41467-018-04576-z. Dec.
[51] J. Yao, L.V. Wang, Photoacoustic microscopy: photoacoustic microscopy, Laser Photonics Rev. 7 (5) (2013) 758–778, https://doi.org/10.1002/lpor.201200060. Sep.
[52] C. Zhang, K. Maslov, L.V. Wang, Subwavelength-resolution label-free photoacoustic microscopy of optical absorption in vivo, Opt. Lett. 35 (19) (2010) 3195, https://doi.org/10.1364/OL.35.003195. Oct.
[53] K. Maslov, G. Stoica, L.V. Wang, In vivo dark-field reflection-mode photoacoustic microscopy, Opt. Lett. 30 (6) (2005) 625, https://doi.org/10.1364/OL.30.000625. Mar.
[54] K. Maslov, H.F. Zhang, S. Hu, L.V. Wang, Optical-resolution photoacoustic microscopy for in vivo imaging of single capillaries, Opt. Lett. 33 (9) (2008) 929, https://doi.org/10.1364/OL.33.000929. May.
[55] J. Yao, L.V. Wang, Photoacoustic microscopy, Laser Photonics Rev. 7 (5) (2013) 758–778.
[56] S. Hu, L.V. Wang, Photoacoustic imaging and characterization of the microvasculature, J. Biomed. Opt. 15 (1) (2010) 011101, https://doi.org/10.1117/1.3281673.
[57] H. Azhari, Basics of Biomedical Ultrasound for Engineers, John Wiley & Sons, 2010.
[58] C. Zhang, K.I. Maslov, J. Yao, L.V. Wang, In vivo photoacoustic microscopy with 7.6-μm axial resolution using a commercial 125-MHz ultrasonic transducer, J. Biomed. Opt. 17 (11) (2012) 116016, https://doi.org/10.1117/1.JBO.17.11.116016. Nov.
[59] H.F. Zhang, K. Maslov, G. Stoica, L.V. Wang, Functional photoacoustic microscopy for high-resolution and noninvasive in vivo imaging, Nat. Biotechnol. 24 (7) (2006) 848–851, https://doi.org/10.1038/nbt1220. Jul.
[60] L.-D. Liao, et al., Imaging brain hemodynamic changes during rat forepaw electrical stimulation using functional photoacoustic microscopy, NeuroImage 52 (2) (2010) 562–570, https://doi.org/10.1016/j.neuroimage.2010.03.065. Aug.
[61] V. Periyasamy, N. Das, A. Sharma, M. Pramanik, 1064 nm acoustic resolution photoacoustic microscopy, J. Biophotonics 12 (5) (2019), https://doi.org/10.1002/jbio.201800357. May.
[62] M. Moothanchery, M. Pramanik, Performance characterization of a switchable acoustic resolution and optical resolution photoacoustic microscopy system, Sensors 17 (2) (2017) 357, https://doi.org/10.3390/s17020357. Feb.
[63] S. Hu, L.V. Wang, Optical-resolution photoacoustic microscopy: auscultation of biological systems at the cellular level, Biophys. J. 105 (4) (2013) 841–847, https://doi.org/10.1016/j.bpj.2013.07.017. Aug.
[64] S.-L. Chen, L.J. Guo, X. Wang, All-optical photoacoustic microscopy, Photoacoustics 3 (4) (2015) 143–150.
[65] M. Moothanchery, R. Bi, J.Y. Kim, S. Jeon, C. Kim, M. Olivo, Optical resolution photoacoustic microscopy based on multimode fibers, Biomed. Opt. Express 9 (3) (2018) 1190–1197, https://doi.org/10.1364/BOE.9.001190. Feb.
[66] D.-K. Yao, K. Maslov, K.K. Shung, Q. Zhou, L.V. Wang, In vivo label-free photoacoustic microscopy of cell nuclei by excitation of DNA and RNA, Opt. Lett. 35 (24) (2010) 4139–4141.
[67] Y. Zhou, G. Li, L. Zhu, C. Li, L.A. Cornelius, L.V. Wang, Handheld photoacoustic probe to detect both melanoma depth and volume at high speed *in vivo*, J. Biophotonics 8 (11–12) (2015) 961–967, https://doi.org/10.1002/jbio.201400143. Nov.
[68] P. Wang, et al., High-speed intravascular photoacoustic imaging of lipid-laden atherosclerotic plaque enabled by a 2-kHz barium nitrite raman laser, Sci. Rep. 4 (1) (2015) 6889, https://doi.org/10.1038/srep06889. May.
[69] Z. Xu, Q. Zhu, L.V. Wang, In vivo photoacoustic tomography of mouse cerebral edema induced by cold injury, J. Biomed. Opt. 16 (6) (2011) 066020, https://doi.org/10.1117/1.3584847.
[70] Y. Zhou, J. Yao, L.V. Wang, Tutorial on photoacoustic tomography, J. Biomed. Opt. 21 (6) (2016) 061007, https://doi.org/10.1117/1.JBO.21.6.061007. Apr.
[71] G.P. Luke, D. Yeager, S.Y. Emelianov, Biomedical applications of photoacoustic imaging with exogenous contrast agents, Ann. Biomed. Eng. 40 (2) (2012) 422–437.
[72] E.M. Strohm, M.J. Moore, M.C. Kolios, Single cell photoacoustic microscopy: a review, IEEE J. Sel. Top. Quantum Electron. 22 (3) (2016) 137–151, https://doi.org/10.1109/JSTQE.2015.2497323. May.
[73] K. Homan, S. Mallidi, E. Cooley, S. Emelianov, Combined photoacoustic and ultrasound imaging of metal nanoparticles in vivo, Nanoimaging 3 (2010).
[74] S. Kim, Y.-S. Chen, G.P. Luke, M. Mehrmohammadi, J.R. Cook, S.Y. Emelianov, Ultrasound and photoacoustic image-guided photothermal therapy using silica-coated gold nanorods: in-vivo study, 2010 IEEE International Ultrasonics Symposium (2010) 233–236.
[75] X. Yang, S.E. Skrabalak, Z.-Y. Li, Y. Xia, L.V. Wang, Photoacoustic tomography of a rat cerebral cortex in vivo with Au nanocages as an optical contrast agent, Nano Lett. 7 (12) (2007) 3798–3802.
[76] S. Yang, et al., Noninvasive monitoring of traumatic brain injury and post-traumatic rehabilitation with laser-induced photoacoustic imaging, Appl. Phys. Lett. 90 (24) (2007) 243902.
[77] J.L.-S. Su, B. Wang, S.Y. Emelianov, Photoacoustic imaging of coronary artery stents, Opt. Express 17 (22) (2009) 19894–19901.
[78] T. Sowers, S. Emelianov, Exogenous imaging contrast and therapeutic agents for intravascular photoacoustic imaging and image-guided therapy, Phys. Med. Biol. 63 (22) (2018) 22TR01, https://doi.org/10.1088/1361-6560/aae62b. Nov.
[79] D.-K. Yao, K. Maslov, K.K. Shung, Q. Zhou, L.V. Wang, In vivo label-free photoacoustic microscopy of cell nuclei by excitation of DNA and RNA, Opt. Lett. 35 (24) (2010) 4139, https://doi.org/10.1364/OL.35.004139. Dec.
[80] C. Zhang, Y.S. Zhang, D.-K. Yao, Y. Xia, L.V. Wang, Label-free photoacoustic microscopy of cytochromes, J. Biomed. Opt. 18 (2) (2013) 020504.
[81] B. Dong, et al., Isometric multimodal photoacoustic microscopy based on optically transparent micro-ring ultrasonic detection, Optica 2 (2) (2015) 169–176.
[82] H.D. Lee, J.G. Shin, H. Hyun, B.-A. Yu, T.J. Eom, Label-free photoacoustic microscopy for in-vivo tendon imaging using a fiber-based pulse laser, Sci. Rep. 8 (1) (2018) 4805, https://doi.org/10.1038/s41598-018-23113-y. Dec.
[83] J. Hui, R. Li, E.H. Phillips, C.J. Goergen, M. Sturek, J.-X. Cheng, Bond-selective photoacoustic imaging by converting molecular vibration into acoustic waves, Photoacoustics 4 (no. 1) (2016) 11–21, https://doi.org/10.1016/j.pacs.2016.01.002. Mar.
[84] K. Maslov, L.V. Wang, Photoacoustic imaging of biological tissue with intensity-modulated continuous-wave laser, J. Biomed. Opt. 13 (2) (2008) 024006, https://doi.org/10.1117/1.2904965.
[85] A. Petschke, P.J. La Rivière, Comparison of intensity-modulated continuous-wave lasers with a chirped modulation frequency to pulsed lasers for photoacoustic imaging applications, Biomed. Opt. Express 1 (4) (2010) 1188, https://doi.org/10.1364/BOE.1.001188. Nov.

[86] W. Zhang, et al., High-resolution, in vivo multimodal photoacoustic microscopy, optical coherence tomography, and fluorescence microscopy imaging of rabbit retinal neovascularization, Light Sci. Appl. 7 (1) (2018) 103, https://doi.org/10.1038/s41377-018-0093-y. Dec.

[87] H.F. Zhang, C.A. Puliafito, S. Jiao, Photoacoustic ophthalmoscopy for in vivo retinal imaging: current status and prospects, Ophthalmic Surg. Lasers Imaging 42 (4) (2011) S106–S115, https://doi.org/10.3928/15428877-20110627-10. Jul.

[88] A. de La Zerda, et al., Photoacoustic ocular imaging, Opt. Lett. 35 (3) (2010) 270–272.

[89] X. Wang, Y. Pang, G. Ku, X. Xie, G. Stoica, L.V. Wang, Noninvasive laser-induced photoacoustic tomography for structural and functional in vivo imaging of the brain, Nat. Biotechnol. 21 (7) (2003) 803–806.

[90] H.F. Zhang, K. Maslov, G. Stoica, L.V. Wang, Imaging acute thermal burns by photoacoustic microscopy, J. Biomed. Opt. 11 (5) (2006) 054033.

[91] V. Ntziachristos, J.S. Yoo, G.M. van Dam, Current concepts and future perspectives on surgical optical imaging in cancer, J. Biomed. Opt. 15 (6) (2010) 066024, https://doi.org/10.1117/1.3523364.

[92] G. Rousseau, A. Blouin, J.-P. Monchalin, Non-contact photoacoustic tomography and ultrasonography for tissue imaging, Biomed. Opt. Express 3 (1) (2012) 16–25.

[93] B. Lengenfelder, et al., Contact-free endoscopic photoacoustic sensing using speckle analysis, J. Biophotonics 12 (12) (2019) e201900130.

[94] T. Berer, E. Leiss-Holzinger, A. Hochreiner, J. Bauer-Marschallinger, A. Buchsbaum, Multimodal noncontact photoacoustic and optical coherence tomography imaging using wavelength-division multiplexing, J. Biomed. Opt. 20 (4) (2015) 046013.

[95] S. Jiao, et al., Photoacoustic ophthalmoscopy for in vivo retinal imaging, Opt. Express 18 (4) (2010) 3967, https://doi.org/10.1364/OE.18.003967. Feb.

[96] P. Beard, Biomedical photoacoustic imaging, Interface Focus 1 (4) (2011) 602–631, https://doi.org/10.1098/rsfs.2011.0028. Aug.

[97] M. Luukkala, P. Heikkila, J. Surakka, Plate wave resonance—A contactless test method, Ultrasonics 9 (4) (1971) 201–208, https://doi.org/10.1016/0041-624X(71)90387-8. Oct.

[98] W.A. Grandia, C.M. Fortunko, NDE applications of air-coupled ultrasonic transducers, in: 1995 IEEE Ultrasonics Symposium. Proceedings. An International Symposium, 1, 1995, pp. 697–709.

[99] D.K. Hsu, Nondestructive testing using air-borne ultrasound, Ultrasonics 44 (2006) e1019–e1024.

[100] A.J. Rogovsky, Development and application of ultrasonic dry-contact and air-contact C-scan systems for nondestructive evaluation of aerospace composites, Mater. Eval. 49 (12) (1991) 1491–1497.

[101] T.E. Gómez Álvarez-Arenas, F.R. Montero de Espinosa, M. Moner-Girona, E. Rodríguez, A. Roig, E. Molins, Viscoelasticity of silica aerogels at ultrasonic frequencies, Appl. Phys. Lett. 81 (7) (2002) 1198–1200, https://doi.org/10.1063/1.1499225. Aug.

[102] D.A. Hutchins, W.M.D. Wright, D.W. Schindel, Ultrasonic measurements in polymeric materials using air-coupled capacitance transducers, J. Acoust. Soc. Am. 96 (3) (1994) 1634–1642, https://doi.org/10.1121/1.410243. Sep.

[103] B. Hosten, D.A. Hutchins, D.W. Schindel, Measurement of elastic constants in composite materials using air-coupled ultrasonic bulk waves, J. Acoust. Soc. Am. 99 (4) (1996) 2116–2123, https://doi.org/10.1121/1.415398. Apr.

[104] C. Li, D.A. Hutchins, R.J. Green, Short-range ultrasonic communications in air using quadrature modulation, IEEE Trans. Ultrason. Ferroelectr. Freq. Control 56 (10) (2009) 2060–2072.

[105] F.-J. García-Diego, J.M. Bravo, J. Pérez-Miralles, H. Estrada, A. Fernández-Navajas, Development of a low-cost airborne ultrasound sensor for the detection of brick joints behind a wall painting, Sensors 12 (2) (2012), https://doi.org/10.3390/s120201299. Art. no. 2, Feb.

[106] D. Sancho-Knapik, T. Gómez Álvarez-Arenas, J.J. Peguero-Pina, E. Gil-Pelegrín, Air-coupled broadband ultrasonic spectroscopy as a new non-invasive and non-contact method for the determination of leaf water status, J. Exp. Bot. 61 (5) (2010) 1385–1391, https://doi.org/10.1093/jxb/erq001. Mar.

[107] D. Sancho-Knapik, H. Calas, J.J. Peguero-Pina, A. Ramos Fernandez, E. Gil-Pelegrin, T.E. Gomez Alvarez-Arenas, Air-coupled ultrasonic resonant spectroscopy for the study of the relationship between plant leaves' elasticity and their water content, IEEE Trans. Ultrason. Ferroelectr. Freq. Control 59 (2) (2012) 319–325, https://doi.org/10.1109/TUFFC.2012.2194. Feb.

[108] E. Corona, J.V. Garcia-Perez, T.E. Gomez Alvarez-Arenas, N. Watson, M.J. W. Povey, J. Benedito, Advances in the ultrasound characterization of dry-cured meat products, J. Food Eng. 119 (3) (2013) 464–470, https://doi.org/10.1016/j.jfoodeng.2013.06.023. Dec.

[109] T.-I. Chiu, H.-C. Deng, S.-Y. Chang, S.-B. Luo, Implementation of ultrasonic touchless interactive panel using the polymer-based CMUT array, 2009 IEEE SENSORS (2009) 625–630, https://doi.org/10.1109/ICSENS.2009.5398325. Oct.

[110] G.R. McMillan, The Technology and Applications of Gesture-based Control, NASA, 1998 no.19990007890.

[111] T.E. Gómez Álvarez-Arenas, J. Camacho, C. Fritsch, Passive focusing techniques for piezoelectric air-coupled ultrasonic transducers, Ultrasonics 67 (2016) 85–93, https://doi.org/10.1016/j.ultras.2016.01.001. Apr.

[112] B.T. Khuri-Yakub, J.H. Kim, C.-H. Chou, P. Parent, G.S. Kino, A new design for air transducers, IEEE 1988 Ultrasonics Symposium Proceedings (1988) 503–506.

[113] T. Yano, M. Tone, A. Fukumoto, Range finding and surface characterization using high-frequency air transducers, IEEE Trans. Ultrason. Ferroelectr. Freq. Control 34 (2) (1987) 232–236.

[114] W. Manthey, N. Kroemer, V. Magori, Ultrasonic transducers and transducer arrays for applications in air, Meas. Sci. Technol. 3 (3) (1992) 249.

[115] D.W. Schindel, D.A. Hutchins, L. Zou, M. Sayer, The design and characterization of micromachined air-coupled capacitance transducers, IEEE Trans. Ultrason. Ferroelectr. Freq. Control 42 (1) (1995) 42–50.

[116] L. Svilainis, A. Chaziachmetovas, V. Dumbrava, Efficient high voltage pulser for piezoelectric air coupled transducer, Ultrasonics 53 (1) (2013) 225–231.

[117] D. Hutchins, P. Burrascano, L. Davis, S. Laureti, M. Ricci, Coded waveforms for optimised air-coupled ultrasonic nondestructive evaluation, Ultrasonics 54 (7) (2014) 1745–1759.

[118] T.H. Gan, D.A. Hutchins, R.J. Green, Swept frequency multiplication (SFM) techniques for improved air-coupled ultrasonic NDE, in: AIP Conference Proceedings, 657, 2003, pp. 620–627, no. 1.

[119] A. Turo, et al., Ultra-low noise front-end electronics for air-coupled ultrasonic non-destructive evaluation, NDT E Int. 36 (2) (2003) 93–100.

[120] R.G. Kolkman, et al., Feasibility of noncontact piezoelectric detection of photoacoustic signals in tissue-mimicking phantoms, J. Biomed. Opt. 15 (5) (2010) 055011.

[121] X.L. Deán-Ben, G.A. Pang, F. Montero de Espinosa, D. Razansky, Non-contact optoacoustic imaging with focused air-coupled transducers, Appl. Phys. Lett. 107 (5) (2015) 051105.

[122] K. Sathiyamoorthy, E.M. Strohm, M.C. Kolios, Low-power noncontact photoacoustic microscope for bioimaging applications, J. Biomed. Opt. 22 (4) (2017) 046001.

[123] J.-P. Monchalin, Optical detection of ultrasound, IEEE Trans. Ultrason. Ferroelectr. Freq. Control 33 (5) (1986) 485–499, https://doi.org/10.1109/T-UFFC.1986.26860. Sep.

[124] S.-L. Chen, Review of laser-generated ultrasound transmitters and their applications to all-optical ultrasound transducers and imaging, Appl. Sci. (Basel) 7 (1) (2017), https://doi.org/10.3390/app7010025. Art. no. 1, Jan.

[125] B. Dong, C. Sun, H.F. Zhang, Optical detection of ultrasound in photoacoustic imaging, IEEE Trans. Biomed. Eng. 64 (1) (2016) 4–15.

[126] Z. Xie, S.-L. Chen, T. Ling, L.J. Guo, P.L. Carson, X. Wang, Pure optical photoacoustic microscopy, Opt. Express 19 (10) (2011) 9027–9034.

[127] M. Liu, et al., Combined multi-modal photoacoustic tomography, optical coherence tomography (OCT) and OCT angiography system with an articulated probe for in vivo human skin structure and vasculature imaging, Biomed. Opt. Express 7 (9) (2016) 3390–3402, https://doi.org/10.1364/BOE.7.003390. Sep.

[128] Z. Chen, et al., Non-invasive multimodal optical coherence and photoacoustic tomography for human skin imaging, Sci. Rep. 7 (1) (2017), https://doi.org/10.1038/s41598-017-18331-9. Art. no. 1, Dec.

[129] B. Zabihian, et al., In vivo dual-modality photoacoustic and optical coherence tomography imaging of human dermatological pathologies, Biomed. Opt. Express 6 (9) (2015) 3163–3178, https://doi.org/10.1364/BOE.6.003163. Sep.

[130] E.Z. Zhang, J.G. Laufer, R.B. Pedley, P.C. Beard, In vivohigh-resolution 3D photoacoustic imaging of superficial vascular anatomy, Phys. Med. Biol. 54 (4) (2009) 1035–1046, https://doi.org/10.1088/0031-9155/54/4/014. Jan.

[131] S.-L. Chen, Z. Xie, T. Ling, L.J. Guo, X. Wei, X. Wang, Miniaturized all-optical photoacoustic microscopy based on microelectromechanical systems mirror scanning, Opt. Lett. 37 (20) (2012) 4263–4265, https://doi.org/10.1364/OL.37.004263. Oct.

[132] R. Ansari, E.Z. Zhang, A.E. Desjardins, P.C. Beard, All-optical forward-viewing photoacoustic probe for high-resolution 3D endoscopy, Light Sci. Appl. 7 (1) (2018) 75, https://doi.org/10.1038/s41377-018-0070-5. Dec.

[133] S.-L. Chen, Z. Xie, L.J. Guo, X. Wang, A fiber-optic system for dual-modality photoacoustic microscopy and confocal fluorescence microscopy using miniature components, Photoacoustics 1 (2) (2013) 30–35, https://doi.org/10.1016/j.pacs.2013.07.001. May.

[134] E.Z. Zhang, et al., Multimodal photoacoustic and optical coherence tomography scanner using an all optical detection scheme for 3D morphological skin imaging, Biomed. Opt. Express 2 (8) (2011) 2202, https://doi.org/10.1364/BOE.2.002202. Aug.

[135] R.A. Barnes, S. Maswadi, R. Glickman, M. Shadaram, Probe beam deflection technique as acoustic emission directionality sensor with photoacoustic emission source, Appl. Opt. 53 (3) (2014) 511, https://doi.org/10.1364/AO.53.000511. Jan.

[136] R. Nuster, G. Zangerl, M. Haltmeier, G. Paltauf, Full field detection in photoacoustic tomography, Opt. Express 18 (6) (2010) 6288–6299, https://doi.org/10.1364/OE.18.006288. Mar.

[137] R. Nuster, P. Slezak, G. Paltauf, High resolution three-dimensional photoacoustic tomography with CCD-camera based ultrasound detection, Biomed. Opt. Express 5 (8) (2014) 2635–2647.

[138] K.P. Köstli, M. Frenz, H.P. Weber, G. Paltauf, H. Schmidt-Kloiber, Optoacoustic tomography: time-gated measurement of pressure distributions and image reconstruction, Appl. Opt. 40 (22) (2001) 3800–3809, https://doi.org/10.1364/AO.40.003800. Aug.

[139] E. Bossy, S. Gigan, Photoacoustics with coherent light, Photoacoustics 4 (1) (2016) 22–35, https://doi.org/10.1016/j.pacs.2016.01.003. Mar.

[140] D.A. Boas, A.K. Dunn, Laser speckle contrast imaging in biomedical optics, J. Biomed. Opt. 15 (1) (2010) 011109, https://doi.org/10.1117/1.3285504.

[141] C.B. Burckhardt, Speckle in ultrasound B-mode scans, IEEE Trans. Sonics Ultrason. 25 (1) (1978) 1–6.

[142] J.-S. Lee, Speckle analysis and smoothing of synthetic aperture radar images, Comput. Graph. Image Process. 17 (1) (1981) 24–32.

[143] J.M. Schmitt, S.H. Xiang, K.M. Yung, Speckle in optical coherence tomography, J. Biomed. Opt. 4 (1) (1999) 95–106.

[144] B. Lengenfelder, et al., Remote photoacoustic sensing using speckle-analysis, Sci. Rep. 9 (1) (2019) 1–11.

[145] M. Benyamin, H. Genish, R. Califa, A. Schwartz, Z. Zalevsky, N. Ozana, Non-contact photoacoustic imaging using laser speckle contrast analysis, Opt. Lett. 44 (12) (2019) 3110–3113.

[146] C. Buj, J. Horstmann, M. Münter, R. Brinkmann, Speckle-based off-axis holographic detection for non-contact photoacoustic tomography, Curr. Dir. Biomed. Eng. 1 (1) (2015) 356–360.

[147] Z. Guo, L. Li, L.V. Wang, On the speckle-free nature of photoacoustic tomography, Med. Phys. 36 (9Part1) (2009) 4084–4088.

[148] Z. Zalevsky, et al., Simultaneous remote extraction of multiple speech sources and heart beats from secondary speckles pattern, Opt. Express 17 (24) (2009) 21566–21580.

[149] S. Lévêque, A.C. Boccara, M. Lebec, H. Saint-Jalmes, Ultrasonic tagging of photon paths in scattering media:?pArallel speckle modulation processing, Opt. Lett. 24 (3) (1999) 181, https://doi.org/10.1364/OL.24.000181. Feb.

[150] S. Lévêque-Fort, Three-dimensional acousto-optic imaging in biological tissues with parallel signal processing, Appl. Opt. 40 (7) (2001) 1029–1036.

[151] G. Yao, L.V. Wang, Theoretical and experimental studies of ultrasound-modulated optical tomography in biological tissue, Appl. Opt. 39 (4) (2000) 659, https://doi.org/10.1364/AO.39.000659. Feb.

[152] G. Yao, S. Jiao, L.V. Wang, Frequency-swept ultrasound-modulated optical tomography in biological tissue by use of parallel detection, Opt. Lett. 25 (10) (2000) 734, https://doi.org/10.1364/OL.25.000734. May.

[153] J. Li, L.V. Wang, Methods for parallel-detection-based ultrasound-modulated optical tomography, Appl. Opt. 41 (10) (2002) 2079–2084.

[154] C. Buj, M. Münter, B. Schmarbeck, J. Horstmann, G. Hüttmann, R. Brinkmann, Noncontact holographic detection for photoacoustic tomography, J. Biomed. Opt. 22 (10) (2017) 106007, https://doi.org/10.1117/1.JBO.22.10.106007. Oct.

[155] J. Horstmann, H. Spahr, C. Buj, M. Münter, R. Brinkmann, Full-field speckle interferometry for non-contact photoacoustic tomography, Phys. Med. Biol. 60 (10) (2015) 4045.

[156] H. Li, F. Cao, P. Lai, Interferometry-free noncontact photoacoustic detection method based on speckle correlation change, Opt. Lett. 44 (22) (2019) 5481–5484.

[157] U. Sangawa, T. Iwamoto, Y. Kaneko, M. Hashimoto, Palm sized airborne ultrasonic sensor with nanofoam acoustic lens and homodyne interferometer, 2010 IEEE International Ultrasonics Symposium (2010) 1442–1445, https://doi.org/10.1109/ULTSYM.2010.5935546. Oct.

[158] Measurement of In-Plane and Out-of-Plane Ultrasonic Displacements by Optical Heterodyne Interferometry | SpringerLink, 2020 (Accessed May 13, 2020), https://link.springer.com/article/10.1007/BF00565636.

[159] W. Li, X. Yu, Z. Meng, Y. Jin, J. Zhang, Experimental study of balanced optical homodyne and heterodyne detection by controlling sideband modulation, Sci. China Phys. Mech. Astron. 58 (10) (2015) 104201, https://doi.org/10.1007/s11433-015-5718-z. Oct.

[160] M.J. Collett, R. Loudon, C.W. Gardiner, Quantum theory of optical homodyne and heterodyne detection, J. Mod. Opt. 34 (6–7) (1987) 881–902, https://doi.org/10.1080/09500348714550811. Jun.

[161] S. Jacob, C. Johansson, M. Ulfendahl, A. Fridberger, A digital heterodyne laser interferometer for studying cochlear mechanics, J. Neurosci. Methods 179 (2) (2009) 271–277.

[162] E. Zhang, et al., Laser heterodyne interferometric signal processing method based on rising edge locking with high frequency clock signal, Opt. Express 21 (4) (2013) 4638–4652.

[163] G. De Vine, et al., Picometer level displacement metrology with digitally enhanced heterodyne interferometry, Opt. Express 17 (2) (2009) 828–837.

[164] A.J.A. Bruinsma, J.A. Vogel, Ultrasonic noncontact inspection system with optical fiber methods, Appl. Opt. 27 (22) (1988) 4690–4695, https://doi.org/10.1364/AO.27.004690. Nov.

[165] G.A. Massey, An optical heterodyne ultrasonic image converter, Proc. IEEE 56 (12) (1968) 2157–2161.

[166] K. Krzempek, et al., Multi-pass cell-assisted photoacoustic/photothermal spectroscopy of gases using quantum cascade laser excitation and heterodyne interferometric signal detection, Appl. Phys. B 124 (5) (2018) 74, https://doi.org/10.1007/s00340-018-6941-x. May.

[167] K. Krzempek, G. Dudzik, K. Abramski, G. Wysocki, P. Jaworski, M. Nikodem, Heterodyne interferometric signal retrieval in photoacoustic spectroscopy, Opt. Express 26 (2) (2018) 1125–1132, https://doi.org/10.1364/OE.26.001125. Jan.

[168] J. Eom, S.J. Park, B.H. Lee, Noncontact photoacoustic tomography of in vivo chicken chorioallantoic membrane based on all-fiber heterodyne interferometry, J. Biomed. Opt. 20 (10) (2015) 106007.

[169] S.A. Carp, A. Guerra III, S.Q. Duque Jr, V. Venugopalan, Optoacoustic imaging using interferometric measurement of surface displacement, Appl. Phys. Lett. 85 (23) (2004) 5772–5774.

[170] S.J. Park, J. Eom, Y.H. Kim, C.S. Lee, B.H. Lee, Noncontact photoacoustic imaging based on all-fiber heterodyne interferometer, Opt. Lett. 39 (16) (2014) 4903–4906.

[171] J. Eom, J.G. Shin, S. Park, S. Rim, B.H. Lee, An all-fiber-optic combined system of noncontact photoacoustic tomography and optical coherence tomography, Sensors 16 (5) (2016) 734.

[172] C. Tian, et al., Non-contact photoacoustic imaging using a commercial heterodyne interferometer, IEEE Sens. J. 16 (23) (2016) 8381–8388.

[173] T. Berer, A. Hochreiner, S. Zamiri, P. Burgholzer, Remote photoacoustic imaging on solid material using a two-wave mixing interferometer, Opt. Lett. 35 (24) (2010) 4151–4153.

[174] S. Zamiri, B. Reitinger, T. Berer, S. Bauer, P. Burgholzer, Determination of nanometer vibration amplitudes by using a homodyne photorefractive crystal interferometer, Procedia Eng. 5 (2010) 299–302.

[175] T. Honda, T. Yamashita, H. Matsumoto, Optical measurement of ultrasonic nanometer motion of rough surface by two-wave mixing in Bi12SiO20, J. Appl. Phys. 34 (7R) (1995) 3737.

[176] S. Luo, Y. Wang, Y. Luo, C. Fan, Study of two-wave-mixing interferometric method in ultrasonic detection using BSO crystal, 2012 IEEE International Conference on Mechatronics and Automation (2012) 1938–1942.

[177] C.B. Scruby, L.E. Drain, Laser Ultrasonics Techniques and Applications, CRC press, 1990.

[178] P.V. Chitnis, H. Lloyd, R.H. Silverman, An adaptive interferometric sensor for all-optical photoacoustic microscopy, 2014 IEEE International Ultrasonics Symposium (2014) 353–356, https://doi.org/10.1109/ULTSYM.2014.0087. Sep.

[179] A. Hochreiner, J. Bauer-Marschallinger, P. Burgholzer, B. Jakoby, T. Berer, Non-contact photoacoustic imaging using a fiber based interferometer with optical amplification, Biomed. Opt. Express 4 (11) (2013) 2322–2331.

[180] A. Hochreiner, T. Berer, H. Grün, M. Leitner, P. Burgholzer, Photoacoustic imaging using an adaptive interferometer with a photorefractive crystal, J. Biophotonics 5 (7) (2012) 508–517.

[181] D. George, H. Lloyd, R.H. Silverman, P.V. Chitnis, A frequency-domain non-contact photoacoustic microscope based on an adaptive interferometer, J. Biophotonics 11 (6) (2018) e201700278.

[182] B. Yu, A. Wang, Grating-assisted demodulation of interferometric optical sensors, Appl. Opt. 42 (34) (2003) 6824–6829.

[183] J.J. Alcoz, C.E. Lee, H.F. Taylor, Embedded fiber-optic Fabry-Perot ultrasound sensor, IEEE Trans. Ultrason. Ferroelectr. Freq. Control 37 (4) (1990) 302–306, https://doi.org/10.1109/58.56491. Jul.

[184] Y. Wang, C. Li, R.K. Wang, Noncontact photoacoustic imaging achieved by using a low-coherence interferometer as the acoustic detector, Opt. Lett. 36 (20) (2011) 3975–3977.

[185] Z. Chen, S. Yang, Y. Wang, D. Xing, Noncontact broadband all-optical photoacoustic microscopy based on a low-coherence interferometer, Appl. Phys. Lett. 106 (4) (2015) 043701.

[186] J. Liu, Z. Tang, Y. Wu, Y. Wang, Rapid and noncontact photoacoustic tomography imaging system using an interferometer with high-speed phase modulation technique, Rev. Sci. Instrum. 86 (4) (2015) 044904.

[187] S. Park, S. Rim, Y. Kim, B.H. Lee, Noncontact photoacoustic imaging based on optical quadrature detection with a multiport interferometer, Opt. Lett. 44 (10) (2019) 2590–2593.

[188] M.A. Choma, C. Yang, J.A. Izatt, Instantaneous quadrature low-coherence interferometry with 3×3 fiber-optic couplers, Opt. Lett. 28 (22) (2003) 2162, https://doi.org/10.1364/OL.28.002162. Nov.

[189] S. Park, J. Lee, Y. Kim, B.H. Lee, Nanometer-scale vibration measurement using an optical quadrature interferometer based on 3 × 3 fiber-optic coupler, Sensors 20 (9) (2020), https://doi.org/10.3390/s20092665. Art. no. 9, Jan.

[190] Z. Ma, et al., Assessment of microvasculature flow state with a high speed all-optic dual-modal system of optical coherence tomography and photoacoustic imaging, Biomed. Opt. Express 9 (12) (2018) 6103–6115.

[191] J. Lu, Y. Gao, Z. Ma, H. Zhou, R.K. Wang, Y. Wang, In vivo photoacoustic imaging of blood vessels using a homodyne interferometer with zero-crossing triggering, J. Biomed. Opt. 22 (3) (2017) 036002.

[192] Y. Wang, Y. Hu, B. Peng, H. Zhou, Y. Zhao, Z. Ma, Complete-noncontact photoacoustic microscopy by detection of initial pressures using a 3× 3 coupler-based fiber-optic interferometer, Biomed. Opt. Express 11 (1) (2020) 505–516.

[193] J. Yao, When pressure meets light: detecting the photoacoustic effect at the origin, Light Sci. Appl. 6 (6) (2017) pp. e17062–e17062.

[194] P. Hajireza, W. Shi, K. Bell, R.J. Paproski, R.J. Zemp, Non-interferometric photoacoustic remote sensing microscopy, Light Sci. Appl. 6 (6) (2017) pp. e16278–e16278.

[195] P.H. Reza, K. Bell, W. Shi, J. Shapiro, R.J. Zemp, Deep non-contact photoacoustic initial pressure imaging, Optica 5 (7) (2018) 814–820.

[196] K.L. Bell, P.H. Reza, R.J. Zemp, Real-time functional photoacoustic remote sensing microscopy, Opt. Lett. 44 (14) (2019) 3466–3469.

[197] S. Abbasi, et al., All-optical reflection-mode microscopic histology of unstained human tissues, Sci. Rep. 9 (1) (2019) 1–11.

[198] S. Abbasi, K. Bell, P. Haji Reza, Rapid high-resolution mosaic acquisition for photoacoustic remote sensing, Sensors 20 (4) (2020) 1027.

[199] S. Abbasi, et al., Chromophore selective multi-wavelength photoacoustic remote sensing of unstained human tissues, Biomed. Opt. Express 10 (11) (2019) 5461–5469.

[200] K.L. Bell, P. Hajireza, R.J. Zemp, Coherence-gated photoacoustic remote sensing microscopy, Opt. Express 26 (18) (2018) 23689–23704.

[201] E.I. Galanzha, E.V. Shashkov, P. Spring, J.Y. Suen, V.P. Zharov, In vivo, non-invasive, label- free detection and eradication of circulating metastatic melanoma cells using two-color photoacoustic flow cytometry with a diode laser, Cancer Res. 69 (20) (2009) 7926–7934, https://doi.org/10.1158/0008-5472.CAN-08-4900. Oct.

[202] W. Li, et al., Gold nanocages covered with thermally-responsive polymers for controlled release by high-intensity focused ultrasound, Nanoscale 3 (4) (2011) 1724–1730, https://doi.org/10.1039/c0nr00932f. Apr.

[203] M.E. van Raaij, M. Lee, E. Chérin, B. Stefanovic, F.S. Foster, Femtosecond photoacoustics: integrated two-photon fluorescence and photoacoustic microscopy, in: Photons Plus Ultrasound: Imaging and Sensing 2010, 7564, 2010, p. 75642E, https://doi.org/10.1117/12.841021. Feb.

[204] Y. Wang, K. Maslov, C. Kim, S. Hu, L.V. Wang, Integrated photoacoustic and fluorescence confocal microscopy, IEEE Trans. Biomed. Eng. 57 (10) (2010) 2576–2578, https://doi.org/10.1109/TBME.2010.2059026. Oct.
[205] X. Zhang, et al., Simultaneous dual molecular contrasts provided by the absorbed photons in photoacoustic microscopy, Opt. Lett. 35 (23) (2010) 4018–4020. Dec.
[206] J.G. Laufer, et al., In vivo preclinical photoacoustic imaging of tumor vasculature development and therapy, J. Biomed. Opt. 17 (5) (2012) 056016.
[207] R. Nuster, M. Holotta, C. Kremser, H. Grossauer, P. Burgholzer, G. Paltauf, Photoacoustic microtomography using optical interferometric detection, J. Biomed. Opt. 15 (2) (2010) 021307.
[208] Y. Hou, S.-W. Huang, S. Ashkenazi, R.S. Witte, M. O'Donnell, Thin polymer etalon arrays for high-resolution photoacoustic imaging, J. Biomed. Opt. 13 (6) (2008) 064033.
[209] K. Bell, K. Bell, P.H. Reza, Non-contact reflection-mode optical absorption spectroscopy using photoacoustic remote sensing, Opt. Lett. 45 (13) (2020) 3427–3430, https://doi.org/10.1364/OL.394637. Jul.

**Zohreh Hosseinaee** After completing her B.Sc. in Biomedical Engineering, Zohreh received her M.Sc. in photonics engineering from Amirkabir University of Technology (Tehran Polytechnic), Iran. She started her Ph.D. in the Systems Design Engineering department at University of Waterloo in 2016. She has worked in the field of Biphotonic and optical imaging, especially optical coherence tomography (OCT). Her current research interest includes multi-modal optical imaging and image processing.